International Forum on Aeroelasticity and Structural Dynamics
IFASD 2019
9-13 June 2019, Savannah, Georgia, USA

MECHANISMS OF TRANSONIC SINGLE DEGREE OF FREEDOM FLUTTER OF A LAMINAR AIRFOIL

Marc Braune[1] **and Anne Hebler**[1]

[1] DLR - German Aerospace Center
Institute of Aeroelasticity
Bunsenstraße 10, 37073 Göttingen, Germany
Marc.Braune@dlr.de

Keywords: Laminar Airfoil, limit Cycle Oscillation, Transonic Dip, Boundary Layer Transition, Shock Motion

Abstract: Results of a flutter experiment on a CAST 10 supercritical laminar airfoil with an experimentally specified degree of freedom in pitch are presented. On the basis of a selected limit cycle oscillation, the underlying unsteady flow effects are analysed. In addition to a resolution of the movement and the temporal behavior of the laminar-turbulent boundary layer transition as well as the movement of the compression shock, the shock-boundary layer interaction is discussed in detail. An analysis of the energy transfer establishes a connection between the previously discussed flow effects and possible causes for the aeroelastic instability as well as the limitation of the amplitude of the observed LCOs. A phase lead of the boundary layer transition in relation to the shock motion occurs. This is associated with a change of the phase difference between the aerodynamic moment and the pitch motion of the laminar airfoil during the onset and growth of limit cycle oscillation, which contributes significantly to the limitation of the LCO amplitude. In addition, a connection between the movement of the boundary layer transition and a positive energy input into the structure is indicated.

1 INTRODUCTION

Airfoil flutter in transonic flow typically occurs within the so called transonic dip which is related to shock dynamic and shock-boundary layer interaction [1]. These fluid mechanical effects are nonlinear in themselves, so that the transonic flow over an airfoil is inherently nonlinear. Thus, transonic flutter is dominated by these effects and as a result often occurs as limit cycle oscillation (LCO) [2, 3]. Transonic flutter becomes even more complex when a laminar-turbulent boundary layer transition is present and begins to interact with the flow, as it is the case for laminar airfoils. Due to the special airfoil geometry, in particular the maximum thickness moved downstream, laminar airfoils maintain a laminar boundary layer over a large part of the chord. Nevertheless, sooner or later a laminar-turbulent boundary transition occurs, resulting in a change of the flow field. Especially in the vicinity of the characteristic drag bucket of the laminar airfoil the boundary layer transition is very sensitive to small disturbances, so that distinct movements of the boundary layer transition can occur [4–7]. As a result, the boundary layer transition also influences the aeroelastic behavior of laminar airfoils, which raises new questions regarding the aeroelastic stability of this technology.

The DLR Institute of Aeroelasticity pursues a long-term strategy to assess the risk of flutter of laminar airfoils [8]. In several numerical and experimental investigations, the influence of

the laminar-turbulent boundary layer transition on the steady and unsteady aerodynamics of a supercritical CAST 10 laminar airfoil was investigated [4, 5, 9–12]. Thereby it was shown that the aerodynamics, in particular the unsteady one, show pronounced nonlinearities for a free transitional boundary layer. These nonlinearities occur locally in the vicinity of the drag bucket of the CAST 10 laminar airfoil and largely disappear for a fully turbulent inflow or a fixed transition. In addition to the studies conducted to investigate the aerodynamics of the laminar airfoil, a 2D flutter test with a heave and a pitch degree of freedom (DOF) was performed to estimate the effect of boundary layer transition on the flutter stability [13]. For a free transitional boundary layer, the transonic dip of the CAST 10 laminar airfoil became deeper and was shifted to lower Mach numbers in comparison to a fully turbulent one. Thus a destabilizing effect of the boundary layer transition occurred, which was confirmed by numerical results [9–11]. Furthermore, the flutter behavior was affected by the boundary layer state as well. Only for a free transitional boundary layer, LCOs were observed that oscillated with almost one degree of freedom (1-DOF) in pitch. These LCOs showed similarities to the 1-DOF LCO observed in flutter tests on the NLR 7301 airfoil presented in [2].

1-DOF flutter is a well-known phenomenon that can occur at the bottom of the transonic dip and differs from the classic 1-DOF pitch flutter in subsonic flow [3, 14–16]. In 2D flutter experiments, 1-DOF LCOs were observed for a free boundary layer transition [17] as well as for a fixed transition [2]. Further aeroelastic instabilities or oscillations with nearly one degree of freedom were observed by [18–20]. Other comparable instabilities or 1-DOF flutter often occur as frequency lock-in phenomena in connection with shock buffet [21]. The underlying mechanisms have recently been attributed to a coupling between a structural mode and an unstable fluid mode [22, 23].

For a more precise identification of the underlaying mechanism of the above mentioned flutter behavior of the CAST 10 laminar airfoil, a second 2D flutter experiment was performed [24]. An aeroelastic configuration with two experimentally specified degrees of freedom heave and pitch was investigated, whereby the LCOs observed in the first flutter experiment occurred again. In the further progress of the flutter test, the heave DOF was locked, thus the 2-DOF configuration was reduced to a configuration with one degree of freedom in pitch. For this 1-DOF configuration LCOs in pitch were observed as well. For higher Mach numbers, these limit cycles became unstable and flutter with rapidly increasing amplitudes occurred that had to be stopped before mechanical damage was caused. Further (nested) LCOs were therefore not detected [2, 25, 26]. However, as with 2-DOF, the 1-DOF instabilities are also directly linked to a free transitional boundary layer since they occurred in the vicinity of the drag bucket of the CAST 10 laminar airfoil and vanish for a turbulent inflow. It is therefore assumed that the complex interaction of shock and boundary layer transition seems to be the reason for these LCOs.

The present paper discusses the mechanism of the observed transonic LCOs for the 1-DOF configuration of the CAST 10 laminar airfoil in two ways. On the one hand, aerodynamic resonances are presented in order to provide a basis for discussion of possible causal effects with the observed flutter behavior, i.e. possible lock-in phenomena or unstable fluid mode interactions. On the other hand, one LCO is analyzed with respect to the occurring shock motion, the motion of the laminar-turbulent boundary layer transition, the interaction of both, and finally the energy transfer between the structure and the flow. This together aims at enabling an identification of the flow processes which lead to the energy input but also to the amplitude limitation of the LCO. This is discussed in detail at the end of the present paper. So, the

paper will contribute to explain the occurrence of the observed LCOs on the laminar airfoil in transonic flow and to further increase the knowledge about the effect of the boundary layer transition on the aeroelastic stability.

2 EXPERIMENTAL METHODOLOGY

The presented results were obtained in 2D wind tunnel tests on a CAST 10 supercritical laminar airfoil model (chord $c = 0.3$ m and span $s = 0.997$ m), carried out in the Transonic Wind Tunnel Goettingen (DNW-TWG). Forced pitching motion tests and a flutter test with one experimentally specified degree of freedom in pitch were conducted. The data evaluated and analyzed here were measured at a Mach number of $\mathrm{Ma} = 0.73$ and a Reynolds number of $\mathrm{Re} \approx 2 \cdot 10^6$ for a boundary layer with free transition, hence, without transition tripping.

An overview of the experimental setup for forced motion tests, with detailed information on the test rig can be found in [4, 5]. In the process of the experiment, steady lift and momemt curves, drag polars, frequency sweeps and pitch oscillations with varying amplitudes and frequencies were measured. The latter are used for the investigation of aerodynamic resonances (see section 3.1.1). The experimental setup of the flutter test is already described in detail in [6, 24]. The application of the hot-film anemometry system used to resolve the boundary layer behavior (see section 3.3) is described in [7]. Hereafter, only the most important key points of the flutter test are summarized.

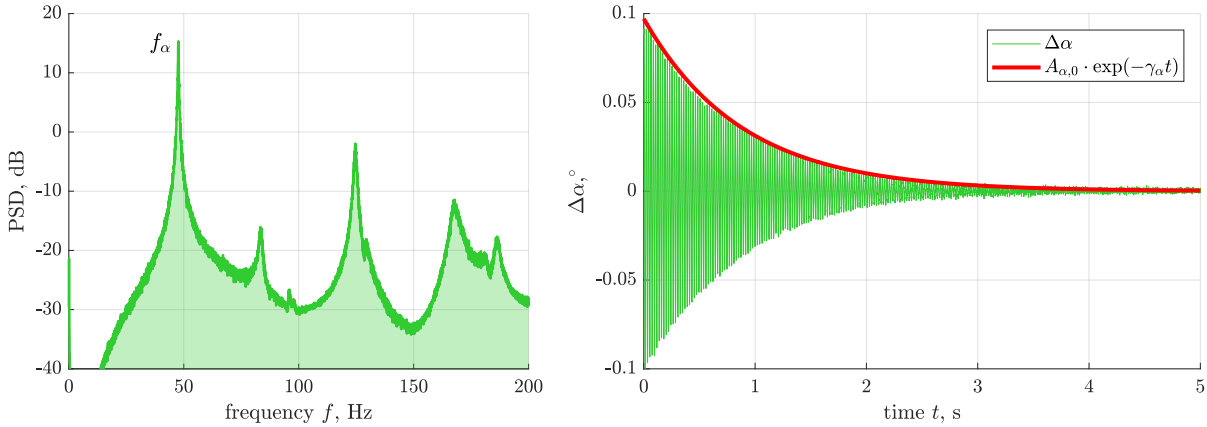

Figure 1: PSD of a selected acceleration sensor (left) and decay curve of the pitch amplitude (right) measured during the vibration test of the aeroelastic 1-DOF configuration.

To provide an aeroelastic system with one degree of freedom, the flutter test rig of the DLR - Institute of Aeroelasticity was used. With the help of a mechanical interlock, the heave degree of freedom was locked. Two torsion springs between which the model was suspended elastically provided a pitch motion of the wind tunnel model around the elastic axis $e = c/4$. The mass moment of inertia related to e, including all parts which perform a pitch oscillation, is $I_\alpha \approx 0.065$ kg·m^2. The wind off eigenfrequency of the 1-DOF configuration, measured during a vibration test, was $f_\alpha = 47.7$ Hz as shown in the power spectral density (PSD) in Fig. 1 on the left side, obtained by an acceleration sensor. Further eigenfrequencies occurring in Fig. 1 belong to structural eigenmodes of the experimental setup. The corresponding damping coefficient is $D_\alpha = \gamma_\alpha/\omega_\alpha \approx 0.39$ % as shown on the right side in Fig. 1 by means of an exemplary decay curve with the corresponding decay coefficient γ_α, also measured during the vibration test. The wind tunnel model and the flutter test rig were equipped with sensors to record unsteady

aerodynamic forces, pressure distributions, boundary layer information and the motion of the airfoil. The angle of attack α was thereby measured by laser triangulators placed outside of the wind tunnel test section. All data were recorded simultaneously and time-synchronized.

Finally, it should be noted that structural nonlinearities of the flutter test rig, in particular of the spring systems, were largely excluded in further structural tests on the test rig. So, the structure of the aeroelastic test setup can be regarded as linear. Observed nonlinear aeroelastic effects such as LCOs are therefore based on nonlinearities resulting from the aerodynamics itself.

3 RESULTS

The following section is divided into two parts. First results obtained during the force motion test are presented, with an emphasis on aerodynamic resonances. This is followed by a description of the results from a 2D flutter test with one degree of freedom in pitch for which a representative LCO case is analyzed in more detail.

3.1 Aerodynamic resonances

In the following, the resonance effects that occurred in the experimental context of the force pitching motion test on the CAST 10 laminar airfoil are briefly discussed. On the one hand, aerodynamic resonances and oscillations of the aerodynamics are taken into account. On the other hand, wind tunnel resonances are discussed. This is done to distinguish between observed self-excited flutter mechanisms later on, possible resonances or possible frequency lock-in phenomena. However, a detailed examination of these correlations goes beyond the scope of this paper and will be addressed in further investigations.

3.1.1 Aerodynamic resonances occurring on the laminar airfoil

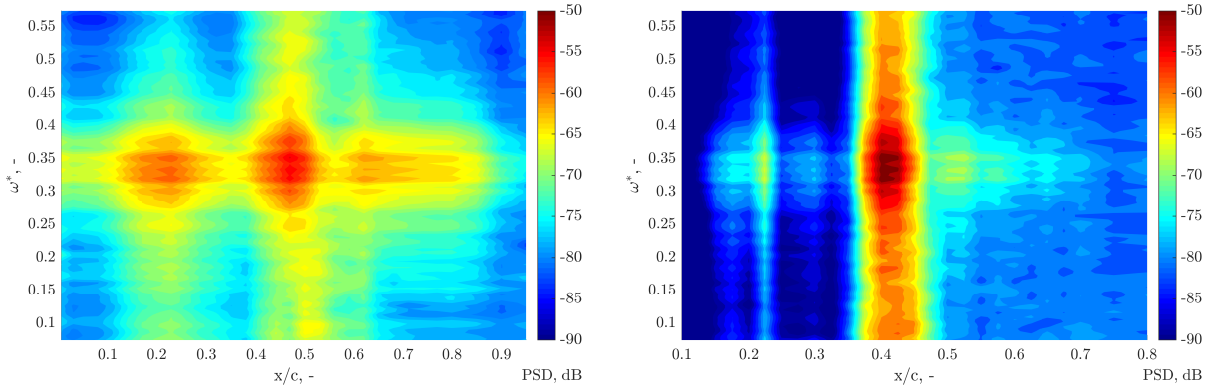

(a) PSD of c_{p_S} (b) PSD of τ_q

Figure 2: Contour plots of the PSD of the pressure distribution c_{p_S} (a) and the quasi-wall shear stress τ_q (b) of the airfoil's suction side, measured at $\mathrm{Ma} = 0.73$ and $\alpha \approx 0°$.

During the measurement of steady lift and pitching moment curves of the CAST 10 laminar airfoil in the vicinity of the characteristic laminar bucket, aerodynamic oscillations occurred around an angle of attack of $\alpha_0 \approx 0°$. The measured pressure distributions showed significant fluctuations of c_p, in particular at Mach numbers of $\mathrm{Ma} = 0.73$ and $\mathrm{Ma} = 0.74$ [24]. For these boundary conditions an unsteady flow field was present around the otherwise steady laminar airfoil model. The PSDs of the pressure distribution of the airfoils's suction side c_{p_S} and the

quasi-wall shear stress τ_q, obtained by the hot-film sensors [7], are shown in Fig. 2(a) and Fig. 2(b), respectively. A general increase in power density of c_{p_S} is observed at $0.4 \lesssim x/c \lesssim 0.6$ for the entire frequency range. This corresponds approximately to the spatial localization of the pressure fluctuations on the suction side of the airfoil for these boundary conditions [24]. The same can be observed in the PSD of the quasi-wall shear stress in the range around $x/c \approx 0.4$. The latter coincides with the position of the laminar-turbulent boundary layer transition [7]. In both cases there is also a marked increase in power density at a reduced frequency[1] of $\omega^* \approx 0.35$ (≈ 45 Hz). This indicates an aerodynamic resonance of the CAST 10 laminar airfoil and is directly related to the observed fluctuations of the pressure distribution.

In addition to the measurement of steady polars, forced pitch oscillations with the CAST 10 laminar airfoil were performed prior to the flutter test. For different Mach numbers the frequency f of the pitch oscillation was varied in the range $13\ Hz \lesssim f \lesssim 73\ Hz$, corresponding to reduced frequencies of $\omega^* \approx 0.1$ up to $\omega^* \approx 0.55$. The mean angle of attack was $\alpha_0 \approx 0°$, the pitch amplitude was kept constant at $\hat{\alpha} \approx 0.1°$. By using the data of the frequency variations,

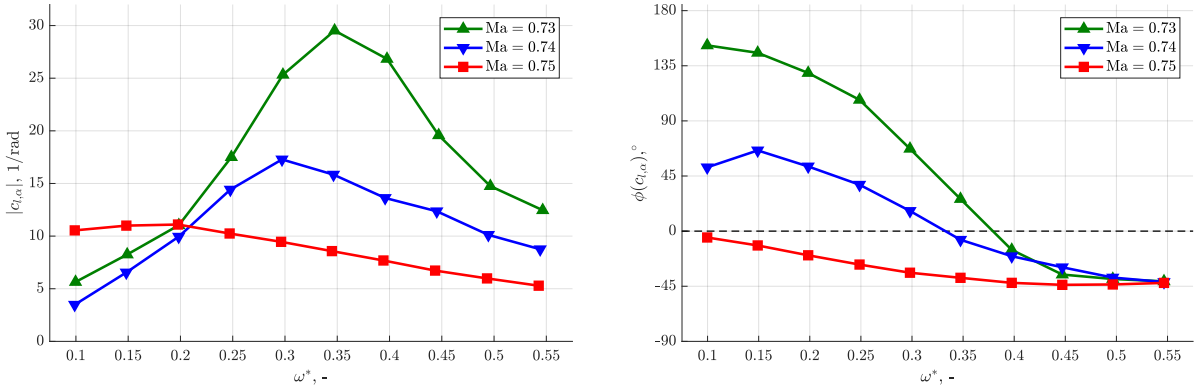

(a) magnitude $|c_{l,\alpha}|$ (b) phase $\phi(c_{l,\alpha})$

Figure 3: Magnitude and phase representation of the lift coefficient derivative $c_{l,\alpha}$.

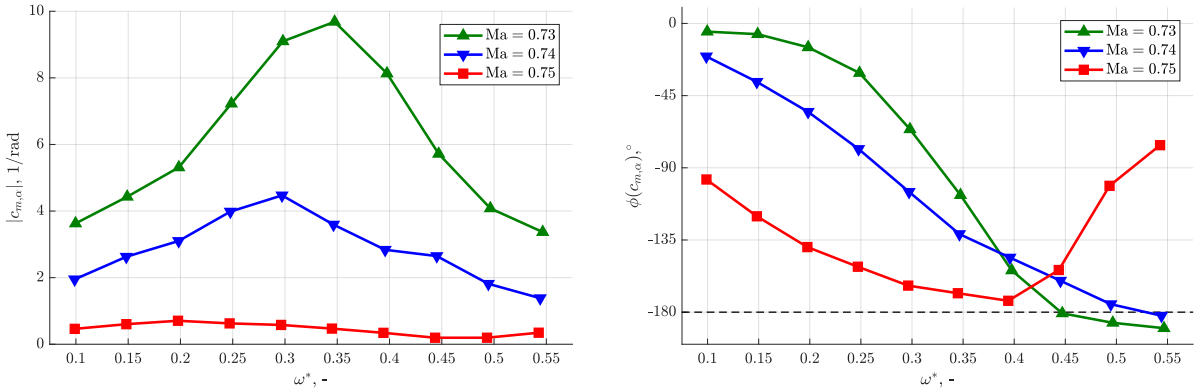

(a) magnitude $|c_{m,\alpha}|$ (b) phase $\phi(c_{m,\alpha})$

Figure 4: Magnitude and phase representation of the moment coefficient derivative $c_{m,\alpha}$.

the aerodynamic derivatives of the lift coefficient $c_{l,\alpha}$ and the moment coefficient $c_{m,\alpha}$ were calculated, based on a H_1-estimator of the transfer function. The results are shown in Fig. 3 and Fig. 4 for $c_{l,\alpha}$ and $c_{m,\alpha}$, respectively. The derivatives are presented by means of their magnitude

[1]The reduced frequency is calculated with the full chord length of the airfoil, so $\omega^* = \frac{\omega\, c}{u_\infty} = \frac{2\pi f c}{u_\infty}$.

$|c_{l,\alpha}|$ or $|c_{m,\alpha}|$ and their phase $\phi(c_{l,\alpha})$ or $\phi(c_{m,\alpha})$. $|c_{l,\alpha}|$ as well as $|c_{m,\alpha}|$ also show a significant maximum around $\omega^* \approx 0.35$ for $\mathrm{Ma} = 0.73$ in agreement with the data in Fig. 2. The maximum values for $|c_{l,\alpha}|$ and $|c_{m,\alpha}|$ both shift with increasing Mach number towards lower frequencies. For $\mathrm{Ma} = 0.74$ the maximum occurs around $\omega^* \approx 0.3$, whereas for $\mathrm{Ma} = 0.75$ none is recognizable. Earlier experimental results already showed a similar behavior and an aerodynamic resonance around $\omega^* \approx 0.2$ for $\mathrm{Ma} = 0.75$ at a slightly increased mean angle of attack of $\alpha \approx 0.2°$ [5]. In numerical investigations a maximum occurred in the lift derivative $|c_{l,\alpha}|$ in a reduced frequency range of about 0.3 to 0.4 for a smaller Mach number $\mathrm{Ma} = 0.72$ and $\alpha_0 = 0°$ [9]. A higher frequency resolution narrowed the frequency range more precisely to a resonance at about $\omega^* \approx 0.35$ and confirmed a shift of the resonance peak to smaller frequencies with increasing Mach number [11]. The significant influence of the mean angle of attack with respect to resonances, thus the associated position within the laminar drag bucket of the laminar airfoil, was also confirmed. However, for a Mach number of 0.73 and $\alpha = 0°$ there was no stable solution of the stationary flow field due to a strongly changing transition position in connection with a periodic occurrence of compression shocks [9]. The development of a new transition model (γ-transition model [27]) has made it possible to prove an aerodynamic resonance even at Ma=0.73, which occurs around $\omega^* \approx 0.45$ and vanishes for a fixed transition location [28]. Nevertheless, the unsteady flow phenomena occurring at the CAST 10 laminar airfoil in the vicinity of the drag bucket around $\mathrm{Ma} \approx 0.73$ are still difficult to capture numerically.

However, in all investigations it was confirmed that aerodynamic resonances are connected to a free boundary layer transition and do not occur for a fully turbulent flow. This is analogous to the 1-DOF flutter mechanism, which also occurs only for a free transitional boundary layer at the laminar airfoil [24]. Altogether the question arises to what extent the occurring resonances are connected to this flutter mechanism. Looking at the effects from the point of view of a possible frequency lock-in, it should be noted that there is a clear discrepancy between the frequencies occurring. The flutter frequencies lie between $0.4 \lesssim \omega^* \lesssim 0.45$ (55 Hz and 60 Hz), whereas the structural wind-off eigenfrequency of the experimentally specified one degree of freedom is below 48 Hz. The maximum of the observed aerodynamic resonances is about $\omega^* \approx 0.35$ at comparable boundary conditions where 1-DOF flutter occurs. Thus one would expect a frequency lock-in rather in the range of the resonance and the structural eigenfrequency, so below the observed flutter frequencies, although the structural frequency changes with increasing Mach number. Nevertheless, based on the available results, a frequency lock-in cannot be ruled out and requires further investigation.

It should also be noted that the derivative of the aerodynamic moment for $\mathrm{Ma} = 0.73$ shows a phase lead ($\phi(c_{m,\alpha}) < -180°$) of c_m for frequencies above about $\omega^* \approx 0.45$, as can be seen in Fig. 4(b), which enables 1-DOF flutter in pitch [29, p. 622]. Further investigations have already shown a similar phase behavior of the aerodynamic moment, but at different Mach numbers or angles of attack [5, 9, 11, 27].

3.1.2 Wind tunnel resonances

All wind tunnel tests on the CAST 10 laminar airfoil were carried out in the adaptive test-section of the DNW-TWG, as described in [24]. An adaptation to the steady flow field of the wind tunnel model at a given mean angle of attack is carried out, thus minimizing remaining wall interference, even for moderately oscillating airfoils [25]. Nevertheless, it is not possible to achieve ideal free flight conditions in the wind tunnel. The occurrence of tunnel wall reflections

in the from of acoustic waves play an essential role [30], in particular in compressible flows and for higher values of the reduced frequency [31]. Thereby, standing wave patterns are formed between tunnel wall and model, when a resonance condition is fulfilled. So, for flutter tests, it must be ensured that wind tunnel resonance frequencies are separated from natural frequencies or dominant flutter frequencies of the aeroelastic system. For a wind tunnel section with closed, solid walls the resonance circular frequencies can be estimated using the method given in [30, 31], which reads

$$\omega_n = (2n-1) \cdot \pi u_\infty \, \frac{\sqrt{1-\mathrm{Ma}^2}}{\mathrm{Ma}} \cdot \frac{1}{2b} \, . \tag{1}$$

ω_n depends on the Mach number Ma, the free stream velocity u_∞ and the half of the wind tunnel test section height b. An evaluation of Eq. (1) at the given boundary conditions where flutter occurs at the laminar airfoil shows that the lowest resonance frequency does not fall below 100 Hz. For the observed 1-DOF flutter cases there are no flutter frequencies above about 60 Hz [24], hence a correlation of both can be excluded.

3.2 Shock motion during LCO

For a more detailed consideration of the mechanisms of 1-DOF flutter on the laminar airfoil, a representative LCO is selected, which has already been discussed in [6, 7, 24]. The time series over three oscillation periods as well as the phase space representation are depicted in Fig. 5. For comparison, a sine wave with the same oscillation frequency of $f_\alpha = 59.2$ Hz (reduced frequency $\omega^* \approx 0.46$) and an amplitude of $\hat{\alpha} = 0.72°$ is plotted as well, showing the nearly sinusoidal airfoil motion in pitch, which was measured by the laser triangulators. In Fig. 5 nine

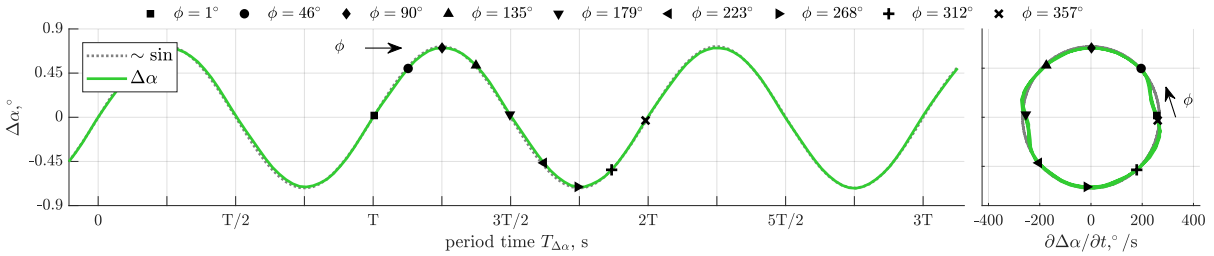

Figure 5: Representative LCO, measured at Ma = 0.73, Re $\approx 2 \cdot 10^6$ and $p_0 = 55$ kPa for a free transitional boundary layer, changed according to [24].

phase angles Φ of one oscillation period are marked by points. The pressure distributions for these nine points indicate a shock motion of nearly 50 % of the chord length along the airfoil suction side during one oscillation period as was presented in [24]. The dynamics of these same points is shown on the left side of Fig. 6, where the temporal and spatial development of the pressure coefficient $c_{p,s}(x,t)$, obtained by the pressure sensors located at the airfoil's suction side, is shown by a contour plot. Red colors mark high negative c_p-values, whereas blue is used for low values. Supersonic areas are enclosed by the critical pressure coefficient $c_p{}^*$ (grey dotted line). For a determination of the shock position the temporal development of the spatial derivative of the pressure distribution $c_{p,s}{}'(x,t) = \partial c_{p,s}/\partial x$, shown on the right side, is used. Compression shocks now lead to a significant increase in pressure, resulting in strong positive gradients colored in red. Fig. 6 (right) shows, that strong positive gradients occur during the LCO in the range $0.7 \lesssim x/c \lesssim 0.8$ and $0.3 \lesssim x/c \lesssim 0.4$ in a periodic sequence. For a more precise quantification of these areas, $c_p(x,t)$ was interpolated linearly and the gradient $\partial c_p/\partial x$ was determined at the intersections with $c_p{}^*$. Based on the sign and the respective gradient value, the position of compression shocks x_s as well as the corresponding shock strength can

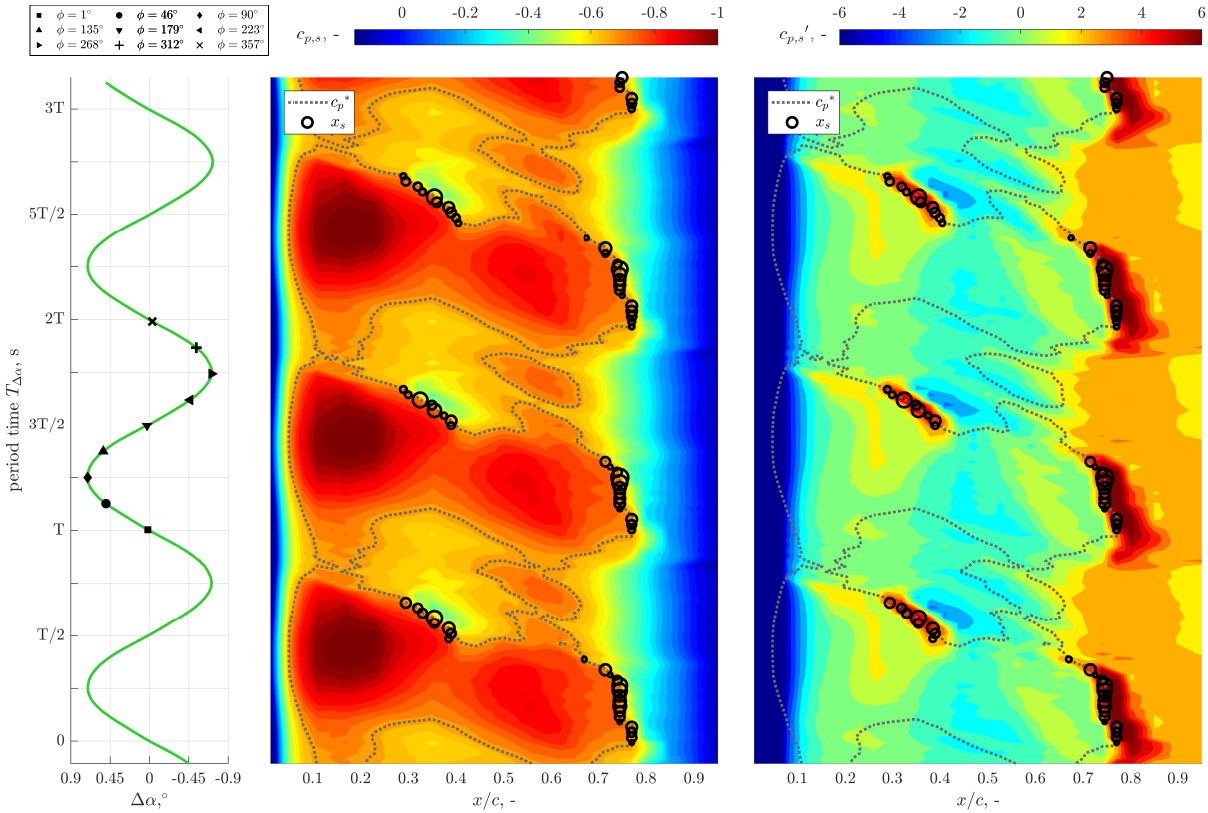

Figure 6: Temporal and spatial development of the pressure distribution of the airfoil's suction side $c_{p,s}(x,t)$ and the spatial gradient $c_{p,s}(x,t)'$ during the LCO. The gray dotted line marks the critical pressure coefficient $c_p{}^*$ and the black circles represent the position of a compression shock.

be largely determined automatically. The shock positions thus obtained are depicted in Fig. 6 by black circles, where the size of the circles scales with the shock strength.

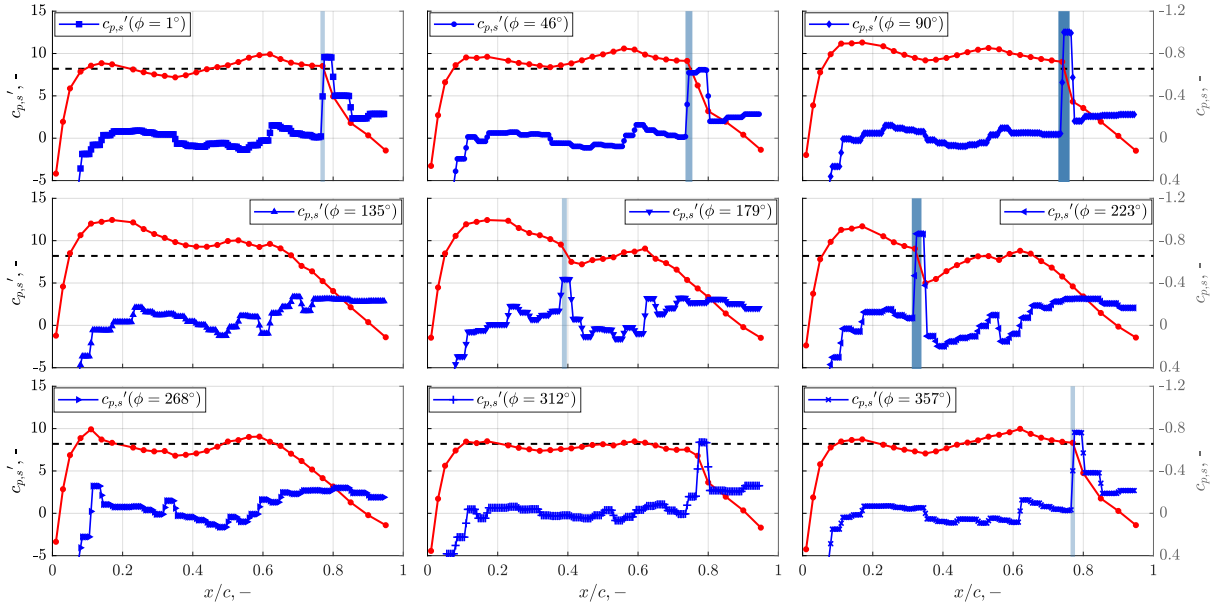

Figure 7: Pressure distributions $c_{p,s}(\phi)$ (red) and the spatial derivative $c_{p,s}{}'$ (blue) for the phase angles marked in Fig. 6. The determined shock position is marked by a blue bar.

To illustrate the determination of the shock position more clearly, the pressure distributions of the airfoil's suction side $c_{p,s}$ as well as the spatial derivatives $c_{p,s}(x,t)'$ for the nine phase angles of the selected LCO period are shown in Fig. 7. The respective shock position obtained is indicated by a blue bar, with the shock strength corresponding to the bar width and transparency. It can be seen that a shock occurs in the range $0.75 \lesssim x_s \lesssim 0.8$ during the upstroke ($\phi \approx 0° \nearrow \phi \approx 90°$) of the laminar airfoil, which increases in strength, but then suddenly disappears with the beginning of the downstroke ($\phi = 135°$). Near the zero crossing of $\Delta\alpha$ the shock reappears upstream at $0.3 \lesssim x_s \lesssim 0.4$ for $\phi \approx 180° \searrow \phi \approx 225°$ and disappears again during the beginning of the upstroke. Occurring supersonic regions ($c_p > {c_p}^*$) where the transition to subsonic velocities is accompanied by a flat pressure increase (for example at $\phi = 135°$), i.e. a small gradient, indicate shock-free recompression and are therefore not identified as a shock.

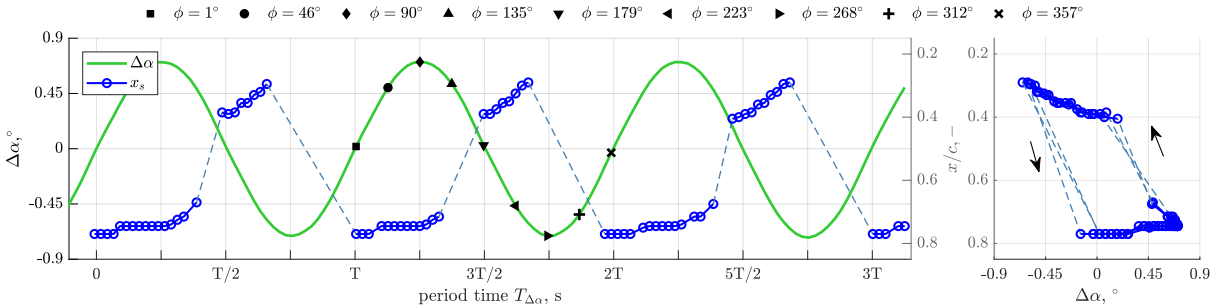

Figure 8: Temporal development of the shock position $x_s(t)$ during the LCO. Dashed lines mark areas where which no shock occurs.

Finally, Fig. 8 shows the motion of the shock position $x_s(t)$ for the entire resolved time range of the considered LCO. Two essential aspects can be identified using this figure. On the one hand, the shock position moves slightly upstream during the upstroke of the laminar airfoil, i.e. with an increase in the angle of attack, what can also be noted in Fig. 6. Consequently, there is an inverse shock motion roughly from $\phi \approx 0°$ to $\phi \approx 90°$, which in turn indicates a detachment of the boundary layer at the trailing edge in this section of the oscillation period. On the other hand, there is a periodic but interrupted shock motion with a changing shock strength. The present shock motion thus resembles a type B shock motion according to [32], but shows besides an interruption of the shock during a part of its backward motion also an interruption during a part of its forward motion. However, the nonlinear behavior of the shock motion is clearly recognizable and leads to nonlinear unsteady lift and moment coefficients, as already discussed in [24]. Furthermore, effects such as trailing edge detachment and type B shock motion are related to the amplitude limitation of LCOs, as discussed in [2,33]. The relationships presented here are further discussed in section 3.5 with regard to a amplitude limitation. The additional motion of the boundary layer and the interaction with the compression shock are described below.

3.3 Boundary layer behavior during LCO

The suction side of the CAST 10 laminar airfoil model is equipped with 26 hot-film sensors, with which the behavior of the boundary layer was resolved along a chordlength of $0.1 \leq x/c \leq 0.8$. A first description of the behavior of the boundary layer during a LCO has already been given in [6]. A more detailed investigation of the laminar-turbulent boundary layer transition motion is presented in [7]. Furthermore, a detailed description of the hot-film anemometry technique and the data evaluation can be found there. In the following, the results

of the boundary layer motion will be described and summarized once more. However, the discussion of a shock-boundary layer interaction, which has already partly taken place in [7], is quantified more precisely here. Using the previously presented results of the shock motion, a correlation with the boundary layer transition movement now allows a more accurate localization of the shock-boundary layer interaction during the LCO.

3.3.1 Motion of the laminar-turbulent boundary layer transition

In [7] a data evaluation method was developed, with which a largely automatic estimation of the unsteady boundary layer transition can be carried out. The transition determination is based on a calculation of the quasi-wall shear stress τ_q [34, 35] and a gradient method, using the signals of the hot-film sensors. The quasi-wall shear stress is physically motivated and directly proportional to the real wall shear stress τ_w, with the exception of deviations when the boundary layer has separated. The latter are caused by the measurement technology used. A boundary layer transition is indicated analogous to τ_w by a significant increase of τ_q, whereby values of the quasi-wall shear stress close to zero indicate a separation of the boundary layer. For the first time, this method enables an analysis of a large amount of unsteady hot-film data and provides valid results even under transonic flow conditions with a shock-boundary layer interaction.

Using this algorithm, the temporal development of the position of the laminar-turbulent boundary layer transition $x_{tr}(t)$ was determined for the selected LCO shown in Fig. 9. It should be

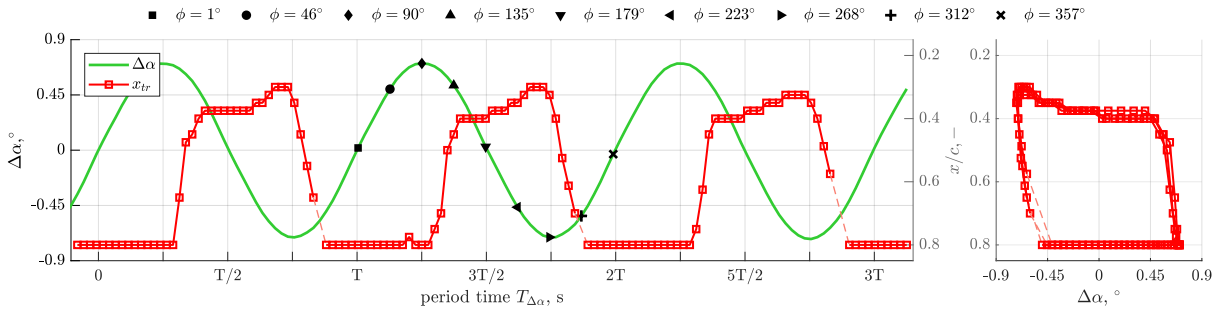

Figure 9: Temporal development of the boundary layer transition position $x_{tr}(t)$ during the LCO. Dashed lines mark areas in which no boundary layer transition occurs, thus a fully laminar boundary layer is present within the sensor range.

noted that the exact estimation of the transition position is limited by the low spatial resolution of 26 hot-film sensors distributed along $0.1 \leq x/c \leq 0.8$. Outside this range, no reliable data on the boundary layer state are available. Furthermore, no spatial extent of the transition process is determined, so that altogether x_{tr} is subject to uncertainty. Nevertheless, Fig. 9 shows that the significant movement of the transition and the behavior of the boundary layer can be resolved during the LCO.

Looking at this behavior for one oscillation period of the laminar airfoil, the position of the laminar-turbulent boundary layer transition does not change during the upstroke of the airfoil ($\phi = 0° \nearrow \phi = 90°$), it remains at an airfoil chord position of $x_{tr} \approx 0.8$. However, it should already be noted here that a slight movement of the transition towards the leading edge of the airfoil occurs, which is not detected by the spatially limited resolution of the hot-film sensors and the evaluation algorithm. A more detailed discussion is given in the following section. With the beginning of the downstroke of the airfoil ($\phi = 90° \searrow \phi = 135°$) a rapid upstream movement of the transition from $x_{tr} \approx 0.8$ to $x_{tr} \approx 0.45$ occurs. This motion decelerates in

the further progress of the downstroke, with the transition moving further towards the leading edge ($x_{tr} \approx 0.3$). Shortly before reaching the reversal point of the model motion ($\phi = 268°$) the transition starts to move downstream again and is located at $x_{tr} \approx 0.7$ for $\phi = 312°$. Subsequently, a complete laminar boundary layer within the sensor range is present for a short period of time, so that no boundary layer transition is detected. In Fig. 9 this area is marked by a dashed line. For larger phase angles (e.g. $\phi = 357°$) the transition position is again $x_{tr} \approx 0.8$.

Overall, a distinct movement of the laminar-turbulent boundary layer transition over more than 50 % of the airfoil's chord can be observed during an oscillation period of the LCO. This periodic movement of the boundary layer transition with a short interruption during the movement downstream has strong similarities to a type B shock motion according to [32]. It can therefore be described as a type B transition movement. Furthermore, a comparison with $\Delta\alpha$ shows that the transition movement is clearly lagging behind the model movement. This is quantified in more detail in the following section in connection with the motion of the shock position.

3.3.2 Shock-boundary layer interaction

The currently received results for the movement of the shock as well as for the movement of the boundary layer transition are shown together in Fig. 10. An interaction of the compression

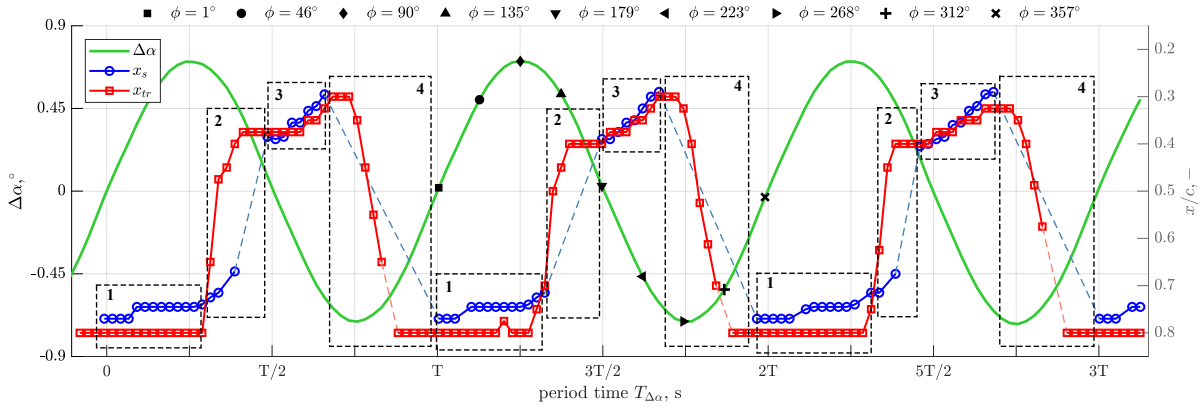

Figure 10: Movement of the shock and transition positions x_s and x_{tr} respectively to illustrate the shock-boundary layer interaction.

shock and the boundary layer transition can thus be directly detected by means of a superposition of both movements. Based on this, four regions can be classified during an oscillation period, which are marked in Fig. 10.

In regions 1 and 3 the position of the shock and the boundary layer transition correlate with each other, whereby in region 3 the shock-boundary layer interaction is directly noticeable. In region 1, x_{tr} and x_s deviate from each other by up to 5 % of the airfoil's chord, whereby especially the transition does not seem to follow the inverse shock motion. As mentioned before, this is due to the limited spatial resolution of the hot-film sensors. As a result, the transition algorithm does not capture the movement of the boundary layer transition accurately enough, which is indeed present and correlates with the shock in this region. Consequently, a shock-boundary layer interaction is also present in region 1. Thus it can be seen that roughly after the zero crossing of the airfoil motion until the upper (region 1) or lower (region 3) reversal point of $\Delta\alpha$ is reached, respectively, shock and transition position correlate. In the regions 2 and 4, which roughly adjoin the reversal points of the movement, there is no correlation between x_{tr} and x_s although the trends of both curves are similar. In region 2, shock and transition position

are temporarily separated from each other up to about 35 % of the airfoil's chord. Between $\phi \approx 130°$ and $\phi \approx 175°$ a shock does not occur at all, as it is the case in the entire region 4. However, it can be clearly seen in both regions that the transition is leading the shock.

These correlations can now be quantified more precisely by the automated evaluation and resolution of the movement of the transition and shock position. Fig. 11 shows the PSDs of the shock movement (top left) and the transition movement (top right). In both cases the first harmonic matches the first harmonic of the airfoil's motion frequency $f_\alpha = 59.2$ Hz. In addition, both x_s and x_{tr} contain further higher harmonic components, which is to be expected given the nonlinear nature of $x_s(t)$ and $x_{tr}(t)$. Based on this, the first harmonics were filtered out and are shown in Fig. 11 together with $\Delta\alpha$. The phase differences of the respective motions are clearly visible, in particular the leading of the transition in relation to the movement of the shock. The phase information φ_x of the first harmonics, calculated on the basis of a transfer function and related to $\Delta\alpha$, are entered in table 1. In addition, the amplitudes of these, so to

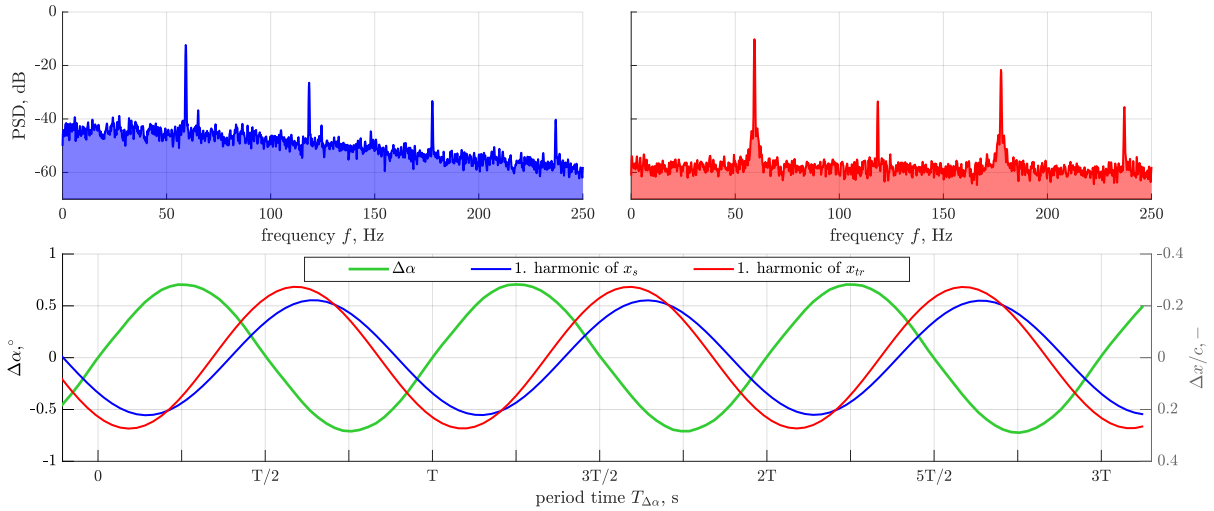

Figure 11: PSDs of the shock (top left) and transition (top right) movement as well as time series of the first harmonics of these movements (bottom).

Table 1: Properties of the first harmonic components of the shock and the transition motion.

LCO	amplitude $\hat{x}$	frequency f_x, Hz	phase φ_x,°
$\Delta\alpha$, °	0.72	59.2	0
x_s/c, -	0.5	59.2	-139
x_{tr}/c, -	0.48	59.2	-121

speak, aerodynamic LCOs, based on the motion of x_s according to Fig. 8 and x_{tr} according to Fig. 9, are listed in table 1 as well. Thus, both the shock movement and the transition lag behind the motion of the laminar airfoil model by $\varphi_{x_s} \approx -139°$ and $\varphi_{x_{tr}} \approx -121°$, respectively. This also shows that there is a phase difference of $\Delta\varphi_{x_{tr},x_s} \approx 18°$ between the movement of the transition and the shock. As can be seen in Fig. 10, particularly in the regions 2 and 4, the transition first leads the shock, which then jumps with some delay to the transition position and correlates with it again. This relationship is further discussed in connection with the amplitude limitation of the LCO in section 3.5.

3.4 Estimation of Energy Transfer during LCO

In addition to the precise quantification of the shock-boundary layer interaction, the question arises which flow effects are associated with a local energy exchange between structure and flow during the LCO. To answer this question, the aerodynamic energy transfer in the mid-section of the laminar airfoil has been calculated. In contrast to previous investigations [25, 36, 37], the entire energy balance of the aeroelastic system was not considered, but only the work W performed by the aerodynamics. If the aeroelastic system is in a stable limit cycle, it can be expected that there is an equilibrium between the aerodynamic work contribution W and the dissipated energy per period due to structural damping [14, 36]. Consequently, the energy supplied per period by the aerodynamics must be positive, so the flow must work on the structure.

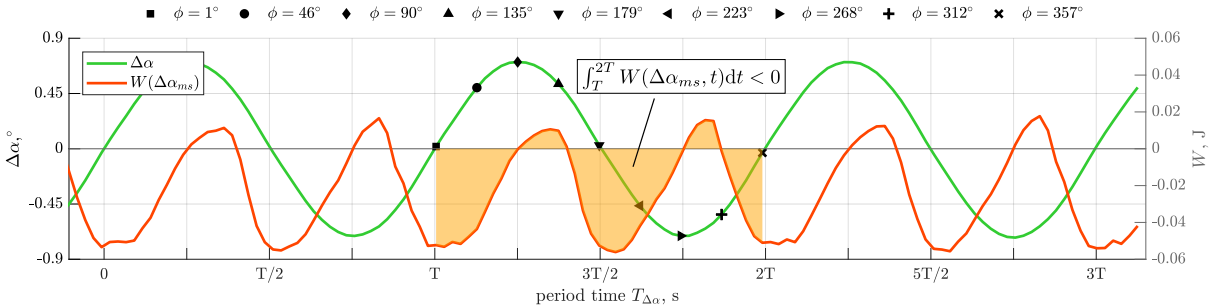

Figure 12: Obtained energy transfer $W(\Delta\alpha_{ms})$ for the represented LCO, whereby for the calculation solely a pitch movement of the laminar airfoil was included. The orange marked area describes the energy transfer over an oscillation period. The green line represents the LCO in pitch $\Delta\alpha$, measured by the laser triangulators.

For the calculation of the energy transfer, first the displacement $\mathrm{d}\vec{r} = \vec{v}(t)\mathrm{d}t$ of a single arc or surface element $\mathrm{d}A$ of the airfoil model during the time increment $\mathrm{d}t$ is determined, related to the airfoil mid-section. The unsteady force $\mathrm{d}\vec{F}(t)$ acting on this surface element is calculated from the measured pressure coefficients to $\mathrm{d}\vec{F} = -q_\infty \left[c_p(t) - \bar{c_p}\right] \mathrm{d}A\, \hat{n}(t)$, with the associated normal vector $\hat{n}(t)$. The work performed by the pressure force per surface element equals $\mathrm{d}W(t) = \mathrm{d}\vec{F}(t) \cdot \mathrm{d}\vec{r}(t)$. The entire work done on the airfoil then results from the integration along the airfoil contour or over all surface elements $W(t) = \oint \mathrm{d}W(t)$. The average work done over a period is then given by $\frac{1}{T}\int_0^T W(t)\ \mathrm{d}t$. A positive sign describes an energy transfer from the flow into the structure, whereas a negative sign describes the energy release by the structure. Fig. 12 shows the energy $W(\Delta\alpha_{ms}, t)$ for the considered LCO, calculated according to the procedure described above. For the determination of the displacement vector $d\vec{r}$ only the motion in pitch $\Delta\alpha_{ms}$ was considered, which was calculated using two acceleration sensors located in the mid-section of the airfoil model. As can be seen immediately, negative work is performed during an LCO period (orange area in Fig. 12, $\int_T^{2T} W(\Delta\alpha_{ms}, t)\ \mathrm{d}t < 0$). The aerodynamic forces respective the pitching moment would therefore contribute to a damping of the motion of the laminar airfoil, which is a clear contradiction to the present LCO.

On the basis of the acceleration sensors integrated in the windtunnel model, the modeshape present during the LCO then has been analyzed in more detail. As has been shown, in addition to the given rigid body degree of freedom in pitch, a structural bending of the wind tunnel model and the experimental setup is also included in the modeshape [2]. This is shown in Fig. 13 for

[2] A comparison of the eigenvectors between the LCO mode $\{\psi_{LCO}\}$ and the experimentally specified 1-DOF

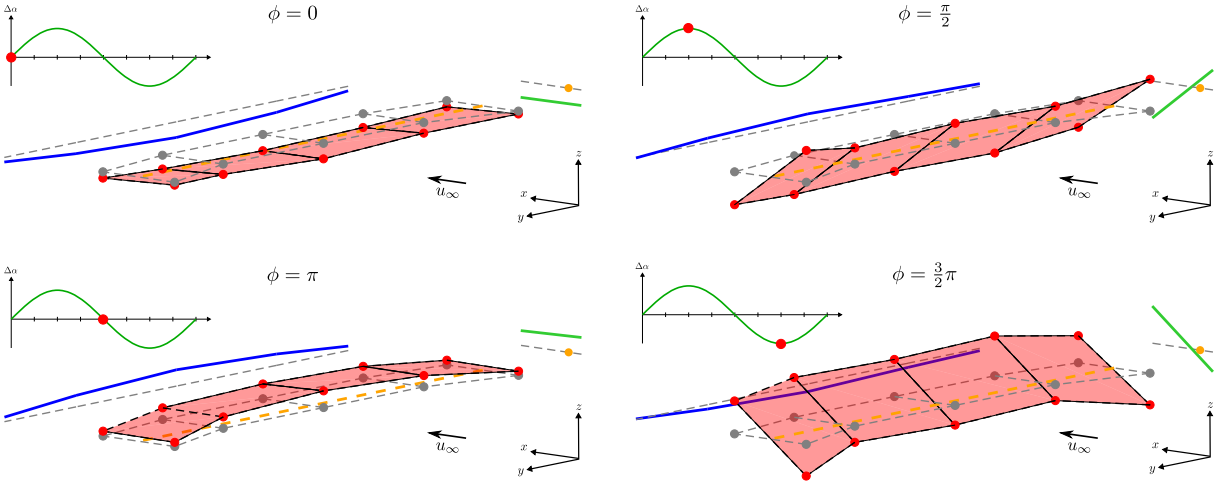

Figure 13: LCO modeshape for four phase angles ϕ of an oscillation period. The rotational axis e is marked by an orange dotted line, while the blue line shows the heave displacement of each acceleration sensor section in relation to e. The green line visualizes the displacement of the mid-section of the model. The grey lines mark the zero deflection in rest.

four phase angles ϕ of a LCO period corresponding to the zero crossings and the upper and lower reversal points. This shows that especially at the zero crossings of $\Delta\alpha(t)$, i.e. for $\phi = 0$ and $\phi = \pi$, there is a deflection of the whole system and thus a vertical shift $h(s,t)$ along the model span s (blue line in Fig. 13). As a result, the motion of the mid-section of the airfoil can be broken down into a combination of a pitch and a heave motion α_{ms} and h_{ms} (green line in Fig. 13), related to the rotational axis e. A re-calculation of the energy input with both α_{ms} and h_{ms} leads to the result shown in Fig. 14. The upper plot now shows the combined motion of the mid-section α_{ms} and h_{ms}, calculated by filtering and integrating the acceleration sensors twice. The middle plot shows the time series of the corresponding aerodynamic coefficients $c_l(t)$ and $c_m(t)$, based on a chordwise integration of the pressure distribution. The lower graph displays the time series of the aerodynamic energy transfer $W(\Delta\alpha_{ms}, \Delta h_{ms}, t)$. An integration over a period now results in a positive energy input, as was to be expected. A direct comparison of the two calculated energy inputs Fig. 12 and Fig. 14 shows that the heave motion due to the bending of the entire aeroelastic system and thus the lift is the most significant factor that feeds energy into the structure, as already observed in earlier flutter tests [25, 36] with the supercritical NLR 7301 airfoil.

The marked influence of the lift becomes even clearer when the total aerodynamic work or the aerodynamic power is broken down into its individual parts. Similar to the presentations in [25], the unsteady components of the aerodynamic power of the lift coefficient $P_l = \partial(h/c)/\partial t\ (c_l - \bar{c_l})$ and of the moment coefficient $P_m = \partial\alpha/\partial t\ (c_m - \bar{c_m})$ as well as the total power $P_l + P_m$ are shown in Fig. 15(a), Fig. 15(b) and Fig. 15(c), represented in the phase space. For reasons of comparability, the heave amplitude has been normalized by the chord length of the airfoil c. The scales of the abscissa and ordinate in Fig. 15 have been normalized by the amplitude of the pitching velocity $\widehat{\partial\alpha/\partial t}$. The power components are further plotted against the normalized pitching velocity $\partial\alpha/\partial t\ /\ \widehat{\partial\alpha/\partial t}$ to distinguish between the upstroke and the

rigid body mode $\{\psi_0\}$ using the Modal Assurance Criterion [38] $MAC = \frac{|\{\psi^*_{LCO}\}^T\ \{\psi_0\}|^2}{\{\psi^*_{LCO}\}^T\{\psi_{LCO}\}\{\psi^*_0\}^T\{\psi_0\}}$ results in a match of approximately 83 %. A participation of a bending within the modeshape may be due to the static coupling of bending and pitching through the position of the center of gravity of the wind tunnel model at $x_{cg}/c \approx 0.41$ and thus behind the center of rotation $e/c = 0.25$.

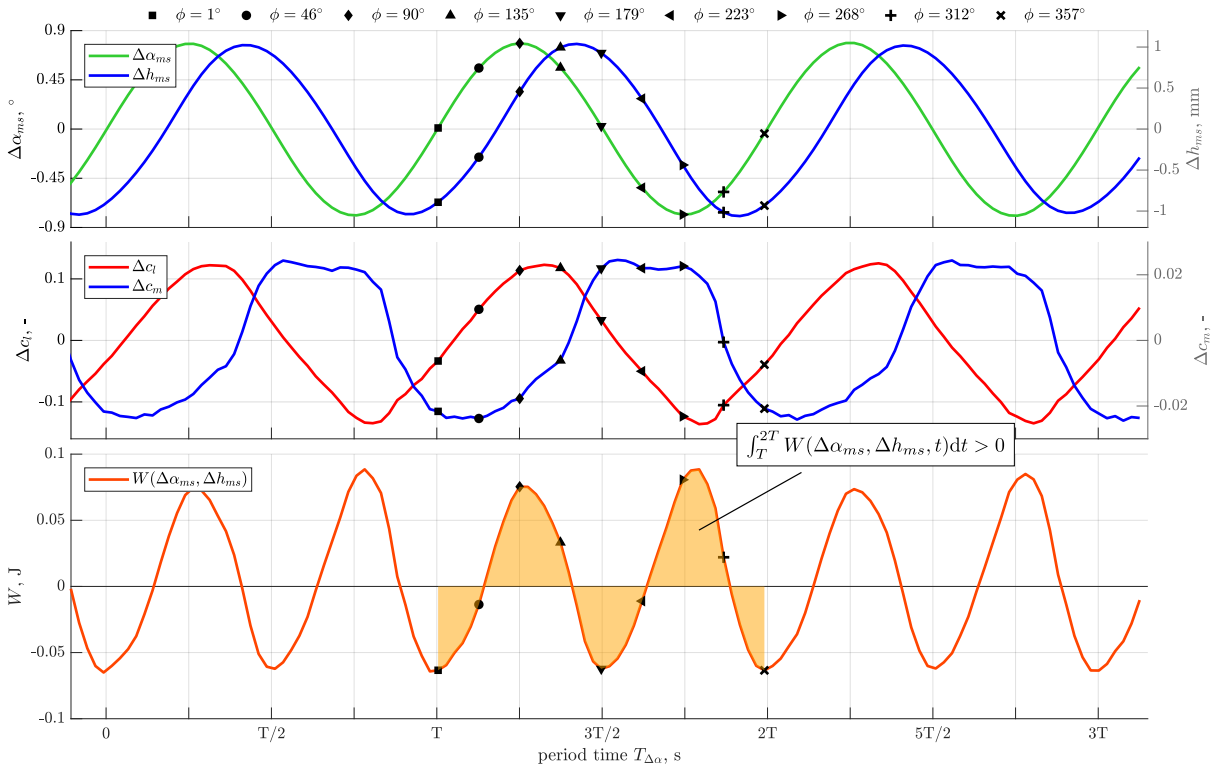

Figure 14: Energy transfer $W(\Delta\alpha_{ms}, \Delta h_{ms})$ (bottom) and lift force and pitching moment coefficients $c_l(t)$ and $c_m(t)$ (middle) for the represented LCO, calculated based on a combined pitch and heave motion of the mid-section (top) of the laminar airfoil. The orange marked area describes the energy transfer over an oscillation period as before.

downstroke of the airfoil model, analogous to [25]. This is schematically illustrated in Fig. 15. Areas where $\partial\alpha/\partial t \;/\; \widehat{\partial\alpha/\partial t}$ is positive correspond to an upstroke motion of the airfoil, negative areas correspond to a downstroke motion. A value around zero corresponds to the upper or lower reversal point, while a value of one (positive or negative) marks the zero crossing of the pitch motion. As can be seen in Fig. 14 and Fig. 15(c), during a LCO period the maximum

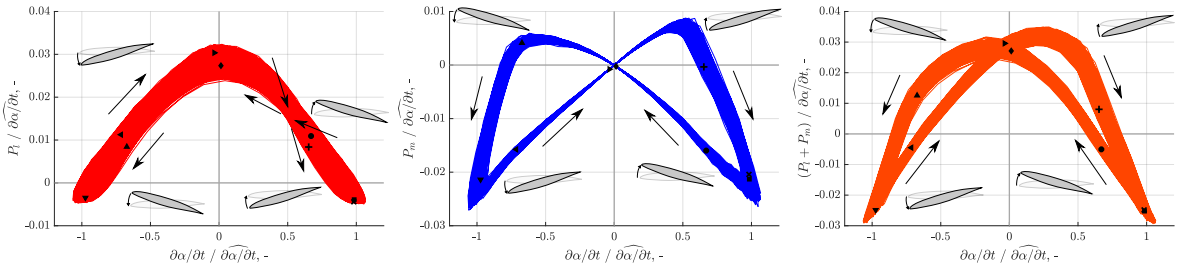

(a) power of lift P_l (b) power of moment P_m (c) aerodynamic power $P_l + P_m$

Figure 15: Aerodynamic power contribution P_l (a) and P_m (b) as well as the total power $P_l + P_m$ (c), represented for the entire time period of the recorded LCO. The positions of the selected phase angles are drawn again with the corresponding markers. The arrows mark the direction of rotation in the phase space.

energy is roughly fed into the structure in the vicinity of the upper as well as the lower reversal point. Around the zero-crossings, in contrast, energy is withdrawn from the system. The consideration of the aerodynamic components in Fig. 15 shows that the lift in particular performs work on the structure over almost the entire range of an oscillation period (Fig. 15(a)). The

aerodynamic moment, on the other hand, damps the LCO over a wide range (Fig. 15(b)) and withdraws energy from the system. Only in a short section behind the upper and lower reversal point, i.e. roughly for ranges $\frac{\pi}{2} \lesssim \phi \lesssim \frac{2\pi}{3}$ and $\frac{3\pi}{2} \lesssim \phi \lesssim \frac{7\pi}{4}$ the moment also supplies energy to the system, which is also shown in Fig. 12.

These correlations can be more accurately quantified by considering the phase relationships between the motion of the laminar airfoil and the aerodynamic forces shown in Fig. 14. The amplitudes and frequencies of these various oscillations as well as the phase difference with respect to the pitch motion of the mid-section are summarized in table 2. As can be seen, there

Table 2: Properties of the limit cycle oscillations.

LCO	amplitude $\hat{x}$	frequency f_x, Hz	phase φ_x,$^\circ$
$\Delta\alpha_{ms}$, $^\circ$	0.80	59.2	0
Δh_{ms}, mm	1.05	59.2	-64
Δc_l, -	0.131	59.2	-18
Δc_m, -	0.024	59.2	-135

is a phase difference of $\Delta\varphi_{c_l,h} = \varphi_{c_l} - \varphi_{h_{ms}} \approx 45^\circ$ between the lift and the heave motion, where the lift leads the heave. As a result, assuming a pure periodic motion of all the components, the direction of the heave motion and the sign of Δc_l are aligned over a period of $3/4T$ thus feeding energy into the structure. Due to the phase difference of $\Delta\varphi_{h,\alpha} = -64^\circ$ between Δh_{ms} and $\Delta\alpha_{ms}$, Δh_{ms} and Δc_l are directed in the opposite direction around the zero crossings of $\Delta\alpha_{ms}$. There energy is extracted from the system, as can be seen in Fig. 15(a). A fairly similar behavior applies to the aerodynamic moment. Here, the phase difference of $\Delta\varphi_{c_m,\alpha} = -135^\circ$ between c_m and pitch leads to energy being withdrawn from the system over a time period of nearly $3/4T$. A positive energy input occurs only in the areas behind the upper and lower reversal points, i.e. around $\frac{\pi}{2} \lesssim \phi \lesssim \frac{2\pi}{3}$ or $\frac{3\pi}{2} \lesssim \phi \lesssim \frac{7\pi}{4}$, as shown in Fig. 12 and already mentioned above. The phase difference between Δh_{ms} and $\Delta\alpha_{ms}$ now leads to an overlapping of the positive energy transfer of both aerodynamic components as well as a reduction of the aerodynamic damping of the moment due to an amplifying effect of the lift. This results in the temporal behavior of the energy transfer between structure and flow, shown in Fig. 14 and Fig. 15(c), and a positive work over one oscillation period of the LCO.

The results of the integrated energy inputs $\oint \mathrm{d}W$ are also shown by a local consideration of the energy transfer. Fig. 16 shows the local energy transfer $\mathrm{d}W$ along the profile contour for the nine selected phase angles of the considered LCO. The size of the markers scales with the amount of energy which is transferred. Green markers indicate an energy transfer from the structure into the flow, i.e. a damping of the model motion. Red markers, on the other hand, mark an energy input from the flow into the structure, thus an amplification of the model motion. As can be seen in Fig. 16, the phase angle ranges ($\frac{\pi}{2} \lesssim \phi \lesssim \frac{2\pi}{3}$ and $\frac{3\pi}{2} \lesssim \phi \lesssim \frac{7\pi}{4}$) in which energy is introduced into the structure are clearly recognizable again. It can also be seen that significant differences in the amount of energy transfer occur essentially only on the profile suction side. The pressure side shows only minor variations, which is related to an only small change of the pressure distribution or the flow effects localized there, as previous investigations have shown [5, 9, 24]. In addition to the periodicity of the integrated energy input $W(t)$ with twice the motion frequency of the LCO (Fig. 14), it can also be seen that at least roughly a symmetry of the local energy inputs $\mathrm{d}W(t)$ is formed over an oscillation period. Thus the local energy distribution for $\phi = 1^\circ$ or $\phi = 357^\circ$ resembles that for $\phi = 179^\circ$. The same applies

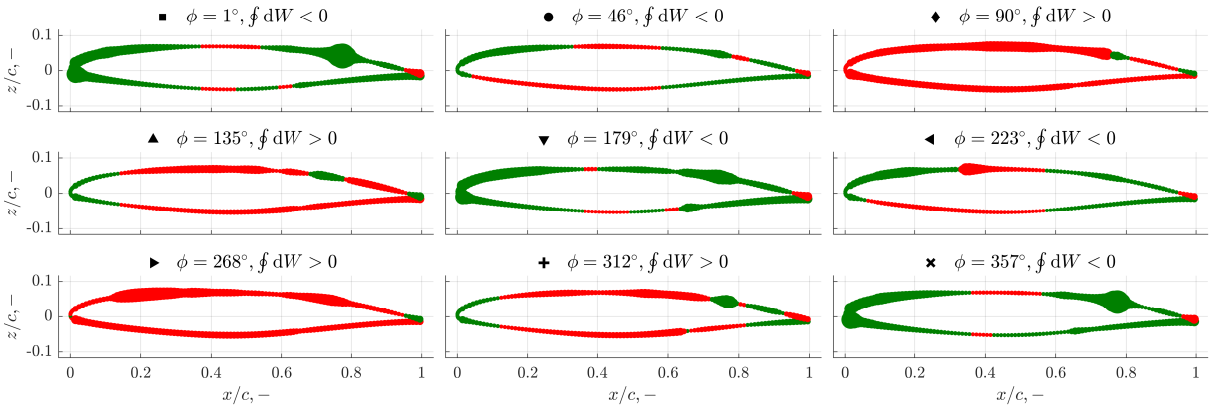

Figure 16: Local energy transfer for the nine phase angles ϕ of the representative LCO.

to $\phi = 46°$ and $\phi = 223°$, $\phi = 135°$ and $\phi = 312°$ as well as $\phi = 90°$ and $\phi = 268°$. The similarity of the integrated energy inputs is already apparent in Fig. 14 by a comparison of $W(\phi_i)$ for the phase angles ϕ_i and $\phi_{i+180°}$, where the latter is shifted by 180 degrees. The local similarity of the energy transfer now may also indicates a local similarity of the underlying flow effects, which therefore also show a periodic behavior, although the pressure distributions differ significantly due to the model motion and the varying angle of attack, as Fig. 7 makes clear.

However, a subsequent more precise identification of the respective flow effects is not always feasible. It is obvious in Fig. 16 that at a phase angle of $\phi = 1°$ and $\phi = 357°$ on the suction side of the laminar airfoil in the range of $0.7 \lesssim x/c \lesssim 0.8$ a significant amount of energy is extracted from the structure. This area correlates with the position of the shock and the laminar separation bubble formed there [7]. So the shock has a damping effect on the LCO at these points, although the shock strength is rather low, as Fig. 7 indicates. In contrast, the already mentioned areas in which energy is introduced roughly correspond to the areas in which a pronounced transition movement occurs, as a comparison with Fig. 9 or Fig. 10 shows. A further discussion of this correlation takes place in the following section.

3.5 Summary Consideration

The aeroelastic instability of the laminar airfoil investigated here now raises the question which mechanism is on the one hand responsible for the instability and on the other hand causes the limitation of the amplitude. The latter question has already been addressed in numerous studies [2, 15, 25, 33, 36]. Thereby the amplitude limitation of the investigated limit cycles was attributed to a transition of the shock motion from type A to type B according to [32] or to a flow separation at the trailing edge combined with an inverse shock motion. All this in turn leads to aerodynamic nonlinearities, which are reflected in particular in the nonlinear behavior of the aerodynamic moment. Both an inverse shock motion in combination with a type B (see section 3.2 and Fig. 8) are also present at the LCO discussed here. A pronounced nonlinear behavior of the aerodynamic moment also exists (see Fig. 14) and has already been discussed in [24]. Consequently, an explanation of the amplitude limitation on the basis of these effects is also obvious here. Nevertheless, a more detailed estimation of the effects responsible for amplitude limitation based on an energy budget analysis as performed in [37] is advised. Thereby, the amplitude limitation of the investigated LCOs was attributed to a nonlinear aerodynamic power defect, where in particular the phase differences between the model motion and the aerodynamic forces have a significant influence. Under the assumption of a purely harmonic oscillation of

the airfoil and the aerodynamic forces

$$\begin{aligned} \Delta\alpha(t) &= \hat{\alpha} \cdot \cos(\omega t + \varphi_\alpha) \quad , & \Delta h(t)/c &= \frac{\hat{h}}{c} \cdot \cos(\omega t + \varphi_h) \, , \\ \Delta c_m(t) &= \hat{c_m} \cdot \cos(\omega t + \varphi_{c_m}) \, , & \Delta c_l(t) \quad &= \hat{c}_l \cdot \cos(\omega t + \varphi_{c_l}) \, , \end{aligned} \tag{2}$$

for the aerodynamic power averaged over a period follows

$$\begin{aligned} \bar{P} &= \frac{1}{T} \int_0^T P_l + P_m \, \mathrm{d}t = \frac{1}{T} \int_0^T \left[\frac{\partial \Delta h/c}{\partial t} \cdot \Delta c_l \right] \, \mathrm{d}t + \frac{1}{T} \int_0^T \left[\frac{\partial \Delta \alpha}{\partial t} \cdot \Delta c_m \right] \, \mathrm{d}t \\ &= -\frac{1}{2} \frac{\hat{h}}{c} \, \hat{c}_l \, \omega \cdot \sin(\varphi_h - \varphi_{c_l}) - \frac{1}{2} \, \hat{\alpha} \, \hat{c_m} \, \omega \cdot \sin(\varphi_\alpha - \varphi_{c_m}) \\ &= -\frac{1}{2} \, \omega \left[\frac{\hat{h}}{c} \, \hat{c}_l \cdot \sin(\Delta\varphi_{h,c_l}) + \hat{\alpha} \, \hat{c_m} \, \cdot \sin(\Delta\varphi_{\alpha,c_m}) \right] \, . \end{aligned} \tag{3}$$

$\bar{P}$ thus depends on the amplitudes of the motion ($\hat{h}$, $\hat{\alpha}$) and the aerodynamic forces ($\hat{c}_l$, $\hat{c_m}$) as well as on the phase differences between heave and lift $\Delta\varphi_{h,c_l}$ as well as between pitch and moment $\Delta\varphi_{\alpha,c_m}$. In the case of linear flutter, these parameters are independent of the amplitude. Nonlinearities now lead to a change of these parameters with increasing amplitude and therefore to the nonlinear aerodynamic power defect, thus an amplitude limitation of the LCO [37].

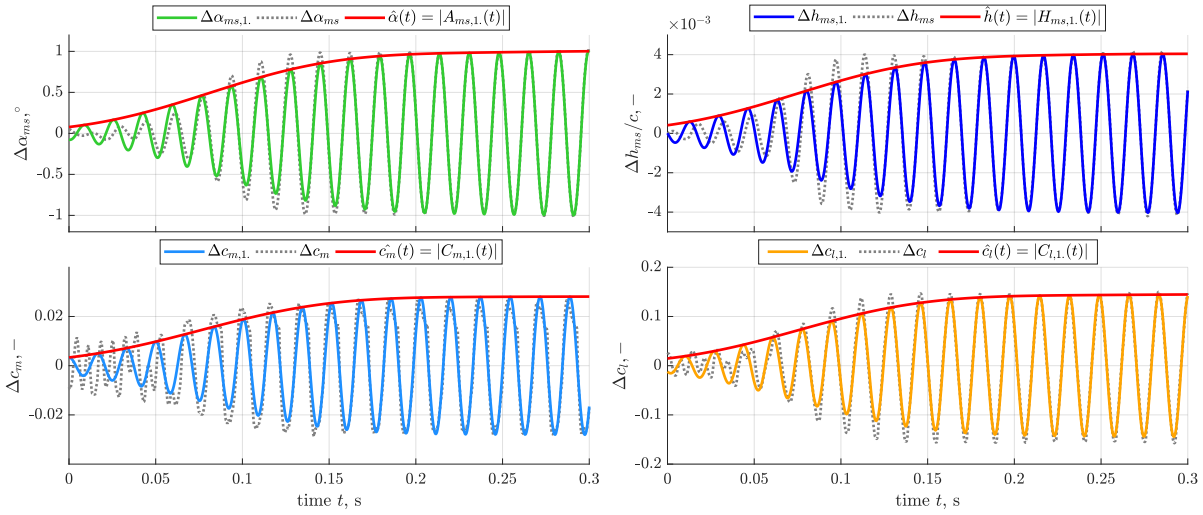

Figure 17: Time series of the amplifying amplitudes of a comparable limit cycle. The motions of the mid-section $\Delta\alpha_{ms}$ and Δh_{ms} as well as the aerodynamic coefficients Δc_l and Δc_m, measured at $\mathrm{Ma} = 0.73$, $p_0 = 55$ kPa, $\mathrm{Re} \approx 2 \cdot 10^6$ and $\alpha_0 \approx 0.06°$, are depicted.

Following this argumentation, Fig. 17 shows the amplitude amplification of a limit cycle comparable to the LCO investigated here[3]. This was recorded at identical flow conditions (1-DOF configuration, $\mathrm{Ma} = 0.73$, $p_0 = 55$ kPa), but at a slightly increased mean angle of attack of $\alpha_0 \approx 0.06°$. Due to the pronounced sensitivity of the flutter mechanism to α_0 [39], this minimal deviation leads to an increased LCO amplitude of $\hat{\alpha}_{ms} \approx 1°$. However, the basic behavior is unchanged and thus comparable with the primary LCO considered in this paper. Fig. 17 depicts the time series of the angle of attack of the middle section $\Delta\alpha_{ms}$ as well as the model bending

[3]To record the ampltiude amplification of the LCO, the aeroelastic system was first fixed with a brake mechanism [24], until this was solved very quickly after adjustment of the stationary flow conditions.

$\Delta h_{ms}/c$ and the aerodynamic coefficients Δc_l and Δc_m. The complete time series (grey dotted line) and the first harmonic components (colored line) are plotted. In addition to the time series, the corresponding envelopes of the first harmonic components of the LCOs are shown in Fig. 17 (red line). These were determined using the analytic function

$$X(t) = x(t) - i\mathcal{H}[x(t)] \tag{4}$$

of the time series $x(t)$, where $\mathcal{H}[x(t)]$ denotes the Hilbert transformation of $x(t)$. The envelope is then given by the magnitude $\hat{x}(t) = |X(t)|$ of the analytic signal.

The envelopes are used to determine the temporal behavior of the amplitudes or their variation for an increasing pitch amplitude. This is shown in Fig. 18 where the trends of the amplitude ratios of the bending $\hat{h}/\hat{\alpha}$ and the aerodynamic coefficients $\hat{c}_l/\hat{\alpha}$ and $\hat{c_m}/\hat{\alpha}$ related to the pitch amplitude $\hat{\alpha}$ are plotted against the time (upper right plot) or against the pitch amplitude $\hat{\alpha}$ itself (lower right plot). Furthermore, the ratio of the lift coefficient to the bending of the mid-section

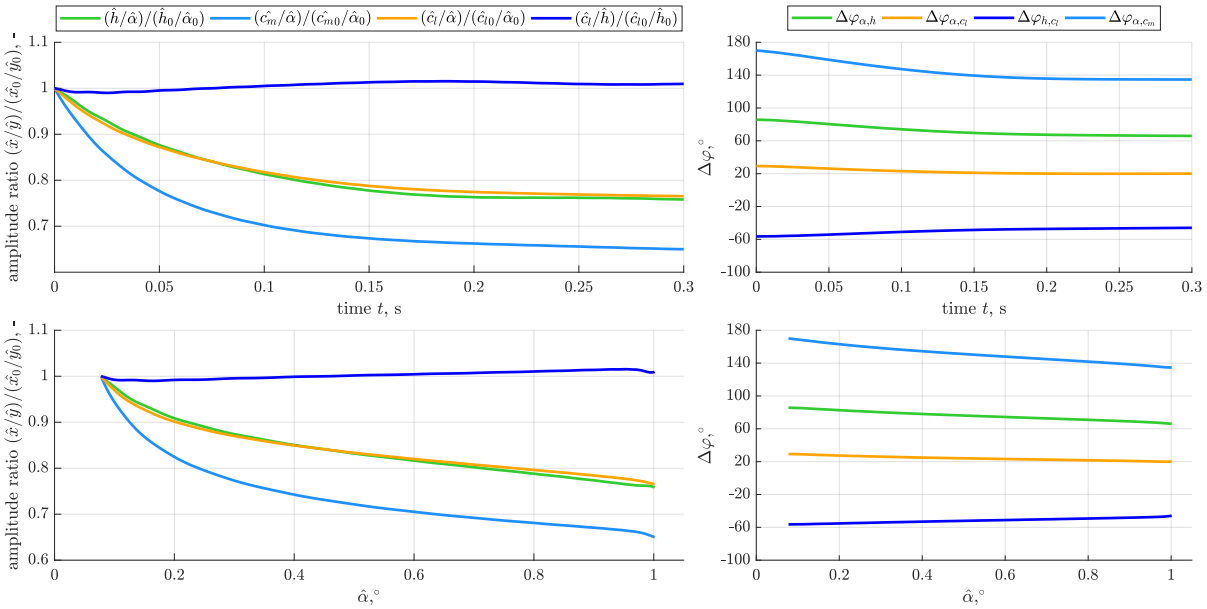

Figure 18: Variation of the amplitudes $\hat{x}$ or amplitude ratios $\hat{x}/\hat{y}$ and change of the phase differences $\Delta\varphi_{x,y}$ as time (upper plot) or as pitch amplitude (lower plots) increases.

$\hat{c}_l/\hat{h}$ is also shown. All ratios are normalized with the initial values $\hat{x}_0/\hat{y}_0$ for $t = 0$ s. In addition, the time-dependent phase differences $\Delta\varphi_{\alpha,x}$[4] of the angle of attack $\alpha_{ms}(t)$ in relation to the respective quantities and the phase difference between the bending and the lift coefficient $\Delta\varphi_{h,c_l}$ are shown in Fig. 18 on the right side. These are also plotted against the pitch amplitude $\hat{\alpha}$. The unsteady phase difference $\Delta\varphi_{x,y} = \varphi_x - \varphi_y$ is also calculated using the analytic function of the time series by

$$\Delta\varphi_{x,y} = \arctan\left[\frac{\mathrm{Im}(X)\,\mathrm{Re}(Y) - \mathrm{Im}(Y)\,\mathrm{Re}(X)}{\mathrm{Re}(X)\,\mathrm{Re}(Y) + \mathrm{Im}(X)\,\mathrm{Im}(Y)}\right] . \tag{5}$$

As Fig. 18 shows, significant differences in the variation of the amplitudes and phase differences occur with increasing angle of attack. On the one hand, it can be seen that the amplitude

[4]It should be noted that the phase differences are not calculated in relation to the motion of the airfoil as usual, thus the signs are inverted.

ratios $\hat{h}/\hat{\alpha}$ and $\hat{c}_l/\hat{\alpha}$ decrease with increasing $\hat{\alpha}$, i.e. during the amplification of the LCO, but exhibit an almost identical behavior. This is also shown by the trend of the amplitude ratio between lift coefficient and bending $\hat{c}_l/\hat{h}$. The ratio remains almost constant, i.e. it is largely independent of the pitch amplitude. In contrast, the aerodynamic moment shows a much greater influence concerning $\hat{\alpha}$. A significant decrease of $\hat{c_m}/\hat{\alpha}$ of more than 30 % with increasing LCO amplitude can be seen. The phase difference $\Delta\varphi_{h,c_l}$ also shows a relatively small change with increasing amplitude, so this one rises about 10°. The change of the phase difference between the pitch and the moment coefficient $\Delta\varphi_{\alpha,c_m}$ is more pronounced. This decreases by more than 34° during the amplification of the LCO.

The effects of these amplitude-related variations are now evident in Fig. 19. Using the estimated time series of the amplitude and phase differences of the LCOs shown in Fig. 17, the aerodynamic power $\bar{P}_l$ and $\bar{P}_m$ averaged over a period as well as the total power $\bar{P}_{\text{ges}} = \bar{P}_l + \bar{P}_m$ were calculated according to eq. (3). The trends of these curves show, that the change of the

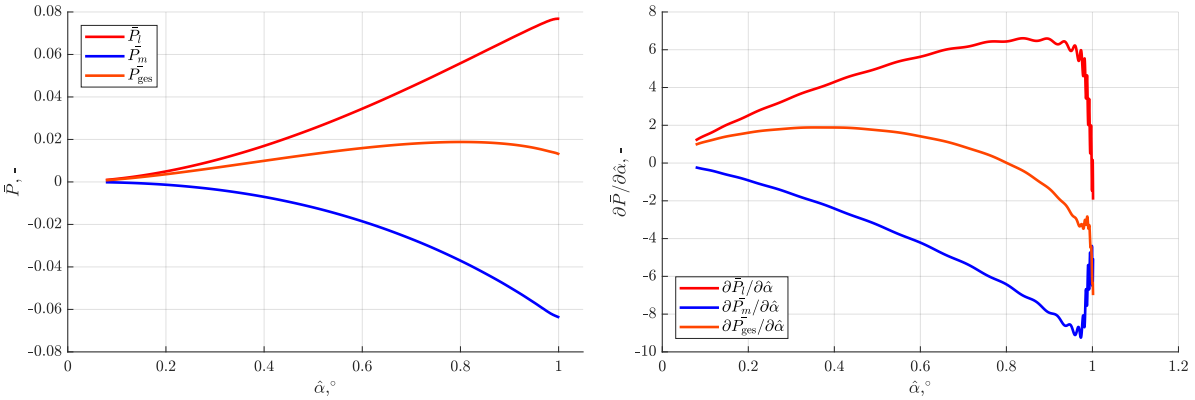

(a) averaged power $\bar{P}$ (b) power gradient $\partial\bar{P}/\partial\hat{\alpha}$

Figure 19: Variation of the estimated mean power components of lift $\bar{P}_l$, moment $\bar{P}_m$ and total power $\bar{P}_{ges}$ with pitch amplitude $\hat{\alpha}$ in (a) and variation of power $\partial\bar{P}/\partial\bar{\alpha}$ depending on $\hat{\alpha}$ in (b).

pitch amplitude has a much stronger effect on the average aerodynamic power of the moment than on the power of the lift. This becomes even clearer when the observations from Fig. 18 and the calculation of the mean aerodynamic power according to eq. (3) are considered more closely. As Fig. 18 shows, the amplitude ratio $\hat{c}_l/\hat{h}$ remains almost constant. The change of the phase difference between c_l and h is also relatively small. Furthermore, it varies in a range of $-55° \lesssim \Delta\varphi_{h,c_l} \lesssim -45°$, resulting in only small changes of $\sin(\varphi_{h,c_l})$ in eq. (3). This relationship is different for the power component of the aerodynamic moment. The amplitude ratio $\hat{c_m}/\hat{\alpha}$ decreases more significantly with increasing pitch amplitude than is found for $\hat{h}/\hat{\alpha}$ and $\hat{c}_l/\hat{\alpha}$. On the other hand, the phase difference $\Delta\varphi_{\alpha,c_m}$ changes markedly with increasing LCO amplitude. Due to the high sensitivity of the sine near the zero crossing ($\Delta\varphi \approx 180°$), this change is much more pronounced, at least for lower amplitudes, since $\Delta\varphi_{\alpha,c_m}$ changes from 170° to 136°. Thus, the behavior is comparable to that already observed in [37].

So, two effects can be identified which are connected with the limitation of the amplitudes of the LCOs considered here. On the one hand there is a reduction of the power input by the lift due to the change of the amplitude ratios $\hat{c}_l/\hat{\alpha}$ and $\hat{h}/\hat{\alpha}$ as well as by the increase of the phase difference $\Delta\varphi_{h,c_l}$. The decisive factor in limiting the amplitude, however, seems to be rather the change in the power input of the aerodynamic moment. Since this has a damping effect and although the amplitude ratio $\hat{c_m}/\hat{\alpha}$ decreases, the decrease of the phase difference $\Delta\varphi_{\alpha,c_l}$

with increasing pitch amplitude leads to an increasing power transfer from the structure into the flow. In Fig. 19(b) this is illustrated by the respective gradients of the mean power with respect to the pitch amplitude $\partial\bar{P}/\partial\hat{\alpha}$. The mean power of the lift (red curve) increases with increasing amplitude until the LCO amplitude of about $\hat{\alpha} \approx 1^\circ$ is reached. The associated gradient also indicates an increasing power input with increasing angle of attack amplitude, but a flattening of the gradient can be recognized already at an early stage. The average power of the moment (blue curve), on the other hand, behaves exactly in an opposite manner. First of all its value is negative, so it has a damping effect. Furthermore, the gradient increases in magnitude, which is a direct consequence of the decrease of the phase difference $\Delta\varphi_{\alpha,c_m}$ or an associated increase of $\sin(\Delta\varphi_{\alpha,c_m})$ with increasing pitch amplitude. At an amplitude of $\hat{\alpha} \approx 0.8^\circ$, for the case shown in Fig. 19, the gradients balance out exactly, so that the average aerodynamic power (orange curve) shows a maximum and begins to decrease in the further process. This decrease then leads to the amplitude limitation of the LCO, since a balance is established between the average total aerodynamic power and the power loss due to friction and dissipation.

As mentioned earlier, the observations of Fig. 17 up to Fig. 19 can be applied to the LCO considered as a priority in this paper. So this indicates that in particular the change of the phase difference between pitch and the aerodynamic moment leads to a limitation of the power consumption of the airfoil from the flow and thus to a limitation of the limit cycle amplitude. This change of the phase relationship is in turn mainly determined by a change of the aerodynamic moment during the amplifying LCO, which is significantly influenced by the motion of the compression shock, shown in Fig. 8, and perhaps also by the formation of a laminar separation bubble. This is confirmed by the fact that the shock motion for the considered LCO oscillates almost in phase with the aerodynamic moment, as a comparison of table 1 and 2 shows. From the temporal resolution of the movement of the boundary layer transition in Fig. 9 or the combined consideration of the shock-boundary layer interaction in Fig. 10 the phase lead of the transition movement becomes apparent. Furthermore, it can be seen that the shock position follows the transition position or that the latter determines the position of the compression shock. It can therefore be concluded that a change in the movement of the transition position interacts with the shock position, which in turn influences the aerodynamic moment. Thus, it can be assumed that the transition movement is responsible for the limitation of the LCO amplitude. Nevertheless, it cannot be ruled out that the type B shock movement here is also responsible for the limitation, as mentioned at the beginning of the section. Either way, in the present case this is in any case massively linked to the boundary layer and its behavior and so the boundary layer or the laminar-turbulent boundary layer transition is again the driving factor.

Finally, the question arises to what extent the boundary layer transition is also responsible for the aeroelastic instabilities of the laminar airfoil considered here. Since in general an aeroelastic system is always composed of a large number of coupled individual systems, it is very difficult to separate them. The answer to this question is therefore an object of future investigation. Nevertheless, a large number of observations show the essential role of the boundary layer transition for the instabilities that occurred, which are summarized here.

- In addition to a shift of the transonic dip for a free transitional boundary layer to lower Mach numbers and also lower stagnation pressures [9–11, 13], flutter mechanisms with essentially one degree of freedom in pitch do not occur for a fully turbulent inflow [24].
- The steady as well as the unsteady aerodynamics of the investigated laminar airfoil show clear nonlinearities, which largely disappear for a fully turbulent inflow [5, 9, 11, 24].
- The same can be observed for the aerodynamic resonances mentioned in 3.1. For a fully

turbulent inflow, the resonances occurring in Fig. 3 and 4 vanish. Although the more precise influence of these effects on the occurring instabilities is further investigated, a direct connection with the boundary layer transition is also recognizable here.

- This is accompanied by a pronounced sensitivity of the position of the boundary layer transition under a variation of the angle of attack [7]. Consequently even small deflections of the structure lead to a movement of the transition, which in turn leads to a further interaction with the aerodynamics, which then again can lead to a motion of the structure and so on.
- As the shock-boundary interaction depicted in Fig. 10 shows, the transition leads the shock movement. The shock places itself on the position of the leading transition and thus contributes significantly to the behavior of the unsteady aerodynamic moment, as previously described. The influence on LCO limitation has already been discussed in detail.
- A comparison of the local consideration of the energy input in Fig. 16 with the resolved shock-boundary interaction in Fig. 10 shows that there is at least a rough temporal correlation of a positive energy input into the structure with the pronounced motion of the boundary layer transition. Although a more detailed resolution does not take place at all, there is also a correlation here.

All in all, these points support the fundamental role of the boundary layer transition. For an even more precise clarification of the influence, numerical as well as experimental concepts are under development, which should make it possible to answer the questions that are still open at the moment.

4 CONCLUDING REMARKS

The present paper discusses in detail the relationships between the boundary layer transition and the aeroelastic instability of the laminar airfoil. For the first time it was possible to establish a more precise and even quantitative measurable connection between the movement of the boundary layer transition and the shock during flutter or LCO. In particular, the amplitude limitation of the LCO could be attributed to the major influence of the boundary layer transition. Furthermore, further essential points could be pointed out which emphasize a destabilizing influence of the transition. For this purpose, the effects of aerodynamic resonances will be addressed more precisely in further investigations. The present results will now also be applied to the large number of different flutter mechanisms that have occurred throughout the transonic dip of the CAST 10 laminar airfoil [13, 24]. Thereby the effect of the Mach number and the stagnation pressure regarding the change of the shock-boundary layer interaction and the flutter mechanisms will be evaluated.

Overall, the results highlighted the potential risks that need to be considered for an assessment of the aeroelastic stability of laminar airfoils and confirmed the points of discussion given in [8]. The increased influence of the boundary layer transition mentioned there as a result of the low Reynolds number ($\sim 2 \cdot 10^6$) in the experiments presented here and the resulting stronger displacement effect of the boundary layer is still an open point of discussion. The transferability to flight realistic Reynolds numbers therefore requires numerical methods and validation experiments under these conditions [8]. However, the available results show that the complexity of an aeroelastic system increases significantly with a laminar inflow and a free boundary layer transition taking place. Both numerical and experimental methods must therefore be able to cover the observed effects, regardless of the Reynolds number.

With regard to the flutter mechanism considered here, a more detailed examination of the movement of the laminar airfoil or the flutter mode showed that a pure 1-DOF flutter mechanism is not present. Even if only one single degree of freedom is defined experimentally, the occurring loads inevitably lead to an additional deflection or elastic model deformation. The existing structural coupling of the wind tunnel model additionally supports this effect. A comparison of the mode shapes between wind on and wind off state shows a rather small deviation, especially since a deflection with an amplitude of about 1 mm only accounts for 0.3 % of the chord length and 0.1 % of the span. However, the energy consideration makes clear that precisely this bending and the heave motion induced by it is essential for a positive energy input and thus for the LCO. However, the influence of the additional heave on the aerodynamics can be considered as marginal, as shown in the appendix. The structural deformation and the aeroelastic influence are of great importance for the further evaluation of the different flutter mechanisms observed on the CAST 10 laminar airfoil, especially for a direct comparison of a 1-DOF and a 2-DOF configuration [24]. This will be closely examined in future studies.

5 REFERENCES

[1] Bendiksen, O. (2001). Transonic flutter and the nature of the transonic dip. In *CEAS/AIAA/AIAE International Forum on Aeroelasticity and Structural Dynamics*, vol. 2. pp. 273–286.

[2] Schewe, G., Mai, H., and Dietz, G. (2003). Nonlinear effects in transonic flutter with emphasis on manifestations of limit cycle oscillations. *Journal of Fluids and Structures*, 18(1). doi:https://doi.org/10.1016/S0889-9746(03)00085-9.

[3] Bendiksen, O. (2011). Review of unsteady transonic aerodynamics: Theory and applications. *Progress in Aerospace Sciences*, 47(2), 135–167. doi:https://doi.org/10.1016/j.paerosci.2010.07.001.

[4] Mai, H. and Hebler, A. (2011). Aeroelasticity of a laminar wing. In *International Forum on Aeroelasticity and Structural Dynamics (IFASD), 26-30 June, Paris, France*.

[5] Hebler, A., Schojda, L., and Mai, H. (2013). Experimental investigation of the aeroelastic behaviour of a laminar airfoil in transonic flow. In *International Forum on Aeroelasticity and Structural Dynamics (IFASD), 24-26 June, Bristol, United Kingdom*.

[6] Braune, M. and Hebler, A. (2019). Sensitivity of single degree of freedom limit cycle flutter of a laminar airfoil and resulting uncertainties of the transonic dip. In A. Dillmann, G. Heller, E. Krämer, C. Wagner, S. Jakirlic, and C. Tropea (Eds.), *New Results in Numerical and Experimental Fluid Mechanics XII*, Notes on Numerical Fluid Mechanics and Multidisciplinary Design. Springer. Accepted for publication.

[7] Braune, M. and Koch, S. (2019). Application of hot-film anemometry to resolve the unsteady boundary layer transition of a laminar airfoil experiencing limit cycle oscillations. In *15th International Conference on Fluid Control, Measurements and Visualization (FLUCOME), May 27-30, Naples, Italy*.

[8] Tichy, L., Mai, H., Fehrs, M., et al. (2017). Risk analysis for flutter of laminar wings. In *International Forum on Aeroelasticity and Structural Dynamics (IFASD), 25-28 June 2017, Como, Italy*.

[9] Fehrs, M. (2013). Influence of transitional flows at transonic mach numbers on the flutter speed of a laminar airfoil. In *International Forum on Aeroelasticity and Structural Dynamics (IFASD), 24-26 June, Bristol, United Kingdom*.

[10] van Rooij, A. C. L. M. and Wegner, W. (2014). Numerical investigation of the flutter behaviour of a laminar supercritical airfoil. In A. Dillmann, G. Heller, E. Krämer, H.-P. Kreplin, W. Nitsche, and U. Rist (Eds.), *New Results in Numerical and Experimental Fluid Mechanics IX*, vol. 124 of *Notes on Numerical Fluid Mechanics and Multidisciplinary Design*. Springer, pp. 33–41. doi:https://doi.org/10.1007/978-3-319-03158-3_4.

[11] Fehrs, M., van Rooij, A. C. L. M., and Nitzsche, J. (2015). Influence of boundary layer transition on the flutter behavior of a supercritical airfoil. *CEAS Aeronautical Journal*, 6(2), 291–303. doi: https://doi.org/10.1007/s13272-014-0147-7.

[12] Hebler, A. and Thormann, R. (2016). Flutter prediction of a laminar airfoil using a doublet lattice method corrected by experimental data. In A. Dillmann, G. Heller, E. Krämer, C. Wagner, and C. Breitsamter (Eds.), *New Results in Numerical and Experimental Fluid Mechanics X*, vol. 132 of *Notes on Numerical Fluid Mechanics and Multidisciplinary Design*. Springer, pp. 445–455. doi:https://doi.org/10.1007/978-3-319-27279-5_39.

[13] Hebler, A. (2017). Experimental assessment of the flutter stability of a laminar airfoil in transonic flow. In *International Forum on Aeroelasticity and Structural Dynamics (IFASD), 25-28 June, Como, Italy*.

[14] Bendiksen, O. O. (2003). Transonic flutter prediction. In *International Forum on Aeroelasticity and Structural Dynamics (IFASD), 4-6 June, Amsterdam, The Netherlands*.

[15] Bendiksen, O. O. (2004). Transonic limit cycle flutter/lco. In *45th AIAA/ASME/ASCE/AHS/ASC Structures, Structural Dynamics & Materials Conference, 19 - 22 April, Palm Springs, California*. doi:10.2514/6.2004-1694.

[16] Bendiksen, O. (2013). Transonic single-degree-of-freedom flutter and natural mode instabilities. In *54th AIAA/ASME/ASCE/AHS/ASC Structures, Structural Dynamics, and Materials Conference, April 8-11, Boston, Massachusetts*. doi:https://doi.org/10.2514/6.2013-1593.

[17] Schewe, G. and Deyhle, H. (1996). Experiments on transonic flutter of a two-dimensional supercritical wing with emphasis on the non-linear effects. In *Proceedings of the Royal Aeronautical Society Conference on Unsteady Aerodynamics, 17-18 July, London, UK*.

[18] Bratt, J., Raymer, W., and Townsend, J. (1962). Measurements of the direct pitching-moment derivatives for two-dimensional flow at subsonic and supersonic speeds and for a wing of aspect ratio 4 at subsonic speeds. Tech. Rep. 3257, Aeronautical Research Council Reports and Memoranda.

[19] Ashley, H. (1980). Role of shocks in the "sub-transonic" flutter phenomenon. *Journal of Aircraft*, 17(3), 187–197. doi:https://doi.org/10.2514/3.57891.

[20] Houwink, R., Kraan, A. N., and Zwaan, R. J. (1982). Wind-tunnel study of the flutter characteristics of a supercritical wing. *Journal of Aircraft*, 19(5), 400–405. doi:https://doi.org/10.2514/3.57409.

[21] Raveh, D. and Dowell, E. (2011). Frequency lock-in phenomenon for oscillating airfoils in buffeting flows. *Journal of Fluids and Structures*, 27(1), 89–104. doi:https://doi.org/10.1016/j.jfluidstructs.2010.10.001.

[22] Gao, C., Zhang, W., and Ye, Z. (2016). A new viewpoint on the mechanism of transonic single-degree-of-freedom flutter. *Aerospace Science and Technology*, 52, 144–156. doi:https://doi.org/10.1016/j.ast.2016.02.029.

[23] Gao, C., Zhang, W., Li, X., et al. (2017). Mechanism of frequency lock-in in transonic buffeting flow. *Journal of Fluid Mechanics*, 818, 528–561. doi:https://doi.org/10.1017/jfm.2017.120.

[24] Braune, M. and Hebler, A. (2018). Experimental investigation of transonic flow effects on a laminar airfoil leading to limit cycle oscillations. In *Applied Aerodynamics Conference, AIAA AVIATION Forum, June 25-29, Atlanta, Georgia*. doi:https://doi.org/10.2514/6.2018-3641.

[25] Dietz, G., Schewe, G., and Mai, H. (2004). Experiments on heave/pitch limit-cycle oscillations of a supercritical airfoil close to the transonic dip. *Journal of Fluids and Structures*, 19, 1-16. doi:https://doi.org/10.1016/j.jfluidstructs.2003.07.019.

[26] Bendiksen, O. (2017). Nested limit cycles in transonic flutter. In *International Forum on Aeroelasticity and Structural Dynamics (IFASD), 25-28 June, Como, Italy*.

[27] Fehrs, M., Nitzsche, J., and Hebler, A. (2017). Cfd-based flutter prediction for high reynolds number flows with free boundary layer transition. In *International Forum on Aeroelasticity and Structural Dynamics (IFASD), 25-28 June, Como, Italy*.

[28] Fehrs, M., Helm, S., and Kaiser, C. (2019). Numerical investigation of unsteady transitional boundary layer flows. In *International Forum on Aeroelasticity and Structural Dynamics (IFASD), 9-13 June, Savannah, Georgia, USA*.

[29] Bisplinghoff, R. L., Ashley, H., and Halfman, R. L. (1996). *Aeroelasticity*. Dover Publications, 1 ed.

[30] Voß, R. (1998). Wind tunnel wall corrections. Report 336, AGARD.

[31] Runyan, H. L., Woolston, D. S., and Rainey, A. G. (1955). Theoretical and experimental investigation of the effect of tunnel walls on the forces on an oscillating airfoil in two-dimensional subsonic compressible flow. Technical Note 3416, National Advisory Commitee for Aeronautics.

[32] Tijdeman, H. and Seebass, R. (1980). Transonic flow past oscillating airfoils. *Annual Review of Fluid Mechanics*, 12, 181-222. doi:https://doi.org/10.1146/annurev.fl.12.010180.001145.

[33] Bendiksen, O. (1992). Role of shock dynamics in transonic flutter. In *Dynamics Specialists Conference, Dallas, TX, USA*. doi:https://doi.org/10.2514/6.1992-2121.

[34] Hodson, H. P. (1985). Boundary-layer transition and separation near the leading edge of a high-speed turbine blade. *Journal of Engineering for Gas Turbines and Power*, 107(1), 127-134. doi:doi:10.1115/1.3239672.

[35] Hodson, H. P., Huntsman, I., and Steele, A. B. (1994). An investigation of boundary layer development in a multistage lp turbine. *Journal of Turbomachinery*, 116(3), 375–383. doi:doi:10.1115/1.2929424.

[36] Dietz, G., Schewe, G., and Mai, H. (2006). Amplification and amplitude limitation of heave/pitch limit-cycle oscillations close to the transonic dip. *Journal of Fluids and Structures*, 22(4), 505–527. doi: https://doi.org/10.1016/j.jfluidstructs.2006.01.004.

[37] van Rooij, A., Nitzsche, J., and Dwight, R. (2017). Energy budget analysis of aeroelastic limit-cycle oscillations. *Journal of Fluids and Structures*, 69, 174–186. doi:https://doi.org/10.1016/j.jfluidstructs.2016.11.016.

[38] Allemang, R. J. (2003). The modal assurance criterion - twenty years of use and abuse. *Sound & Vibration*, 37(8), 14-21.

[39] Braune, M. and Hebler, A. (2019). Hysteretic response of a laminar airfoil undergoing single degree of freedom limit cycle oscillations in transonic flow. In *International Forum on Aeroelasticity and Structural Dynamics (IFASD), 9-13 June, Savannah, Georgia, USA*.

COPYRIGHT STATEMENT

A AERODYNAMIC ASSESSMENT OF THE BENDING MOTION

An analysis of the energy balance during the LCO shows that the observed flutter mechanism of the laminar airfoil is not solely due to a single degree of freedom mechanism in pitch. For an interpretation of the occurring aerodynamic effects, however, the question arises to what extent an additional heave motion due to the observed structural bending has an influence on the aerodynamics involved. As a result of the additionally induced velocity caused by the heave motion, the flow field changes, which in turn results in a change in the effective angle of attack

$$\alpha_{\text{eff}}(t) = \alpha_{ms}(t) + \alpha_h(t) = \alpha_{ms}(t) - \frac{\partial h/\partial t}{u_\infty} \, .$$

Therefore, with the LCO considered here, the additional heave motion with an amplitude of $\hat{h} \approx 1.05$ mm in the mid-section leads to an additional angle of attack $\alpha_h(t)$ with an amplitude of $\widehat{\alpha_h} \approx 0.09°$. The phase relationship between the heave and the pitch motion therefore results in a relative reduction of the angle of attack amplitude from $\widehat{\alpha_{ms}} \approx 0.80°$ by 11 % to $\widehat{\alpha_{\text{eff}}} \approx 0.71°$. The respective parts of the angle of attack are shown in Fig. 20. It also shows that there is a small phase difference between $\alpha_{ms}(t)$ and $\alpha_{\text{eff}}(t)$ of $-3°$, so $\alpha_{\text{eff}}(t)$ lags behind $\alpha_{ms}(t)$.

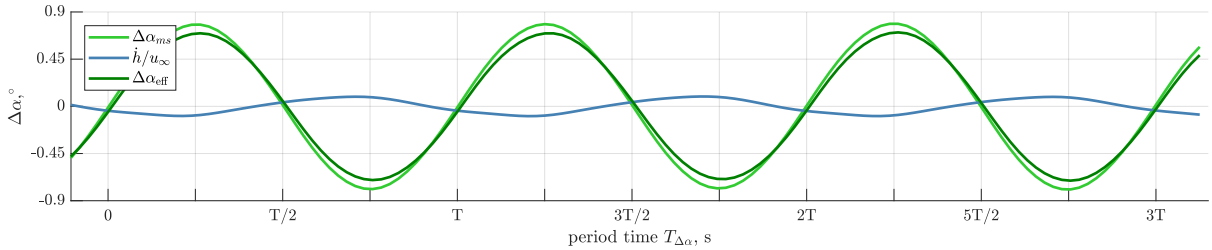

Figure 20: Decomposition of the effective angle of attack $\alpha_{\text{eff}}(t)$ into the parts of the pitch motion $\alpha_{ms}(t)$ and the heave motion $\alpha_h(t) = -\frac{\partial h/\partial t}{u_\infty}$.

The review of the mode shape in Fig. 13 further clarifies that the largest heave amplitudes occur entirely in the mid-section of the airfoil model and decrease as the distance to the mid-section increases. Thus, the influence of the heave motion on the effective angle of attack is also becoming increasingly smaller. A comparison with the unsteady angle of attack $\Delta\alpha(t)$ measured by the laser triangulators (see section 2) shows that the difference in the measured amplitudes of the LCO with $\widehat{\Delta\alpha} \approx 0.72^\circ$ or $\widehat{\Delta\alpha_{\text{eff}}} \approx 0.71^\circ$ is negligibly small and lies within the error intervals. Also the phase difference of both angle of attack measurements with $\approx -2^\circ$ lies within a negligible range within the measurement error.

Overall, the influence of the additionally induced angle of attack due to the bending motion of the airfoil can therefore be classified as rather small with regard to the aerodynamic effects. Furthermore, the differences between the effective angle of attack of the airfoils's mid-section and the angle of attack measured at the model ends using the laser triangulators are negligible.